



The structural basis of Rubisco phase separation in the pyrenoid

Shan He¹, Hui-Ting Chou^{2,3}, Doreen Matthies⁴, Tobias Wunder⁴, Moritz T. Meyer¹, Nicky Atkinson⁵, Antonio Martinez-Sanchez^{6,7}, Philip D. Jeffrey¹, Sarah A. Port¹, Weronika Patena¹, Guanhua He¹, Vivian K. Chen⁸, Frederick M. Hughson¹, Alistair J. McCormick⁵, Oliver Mueller-Cajar⁴, Benjamin D. Engel^{6,9,10}, Zhiheng Yu² and Martin C. Jonikas¹✉

Approximately one-third of global CO₂ fixation occurs in a phase-separated algal organelle called the pyrenoid. The existing data suggest that the pyrenoid forms by the phase separation of the CO₂-fixing enzyme Rubisco with a linker protein; however, the molecular interactions underlying this phase separation remain unknown. Here we present the structural basis of the interactions between Rubisco and its intrinsically disordered linker protein Essential Pyrenoid Component 1 (EPYC1) in the model alga *Chlamydomonas reinhardtii*. We find that EPYC1 consists of five evenly spaced Rubisco-binding regions that share sequence similarity. Single-particle cryo-electron microscopy of these regions in complex with Rubisco indicates that each Rubisco holoenzyme has eight binding sites for EPYC1, one on each Rubisco small subunit. Interface mutations disrupt binding, phase separation and pyrenoid formation. Cryo-electron tomography supports a model in which EPYC1 and Rubisco form a codependent multivalent network of specific low-affinity bonds, giving the matrix liquid-like properties. Our results advance the structural and functional understanding of the phase separation underlying the pyrenoid, an organelle that plays a fundamental role in the global carbon cycle.

The CO₂-fixing enzyme Rubisco drives the global carbon cycle, mediating the assimilation of approximately 100 gigatons of carbon per year¹. The gradual decrease of atmospheric CO₂ over billions of years² has made Rubisco's job increasingly difficult, to the point where CO₂ assimilation limits the growth rate of many photosynthetic organisms³. This selective pressure is thought to have led to the evolution of CO₂-concentrating mechanisms, which feed concentrated CO₂ to Rubisco to enhance growth⁴. Of these mechanisms, the most poorly understood relies on the pyrenoid, a phase-separated organelle⁵ found in the chloroplast of nearly all eukaryotic algae and some land plants (Fig. 1a,b)^{6,7}. The pyrenoid enhances the activity of Rubisco by clustering it around modified thylakoid membranes that supply Rubisco with concentrated CO₂ (refs. ^{8,9}).

For decades, the mechanism for packaging the Rubisco holoenzyme into the pyrenoid remained unknown. Recent work showed that in the leading model alga *Chlamydomonas reinhardtii*, the clustering of Rubisco into the pyrenoid matrix requires the Rubisco-binding protein Essential Pyrenoid Component 1 (EPYC1) (ref. ¹⁰). EPYC1 and Rubisco are the most abundant components of the pyrenoid and bind to each other. Moreover, combining purified EPYC1 and Rubisco produces phase-separated condensates¹¹ that mix internally at a rate similar to that observed for the matrix *in vivo*⁵, suggesting that these two proteins are sufficient to form the structure of the pyrenoid matrix. The sequence repeats in EPYC1 and the eightfold symmetry of the Rubisco holoenzyme led us to hypothesize that EPYC1 and Rubisco each have multiple binding

sites for the other, allowing the two proteins to form a codependent condensate (Fig. 1c)¹⁰.

In this Article, we determined the structural basis that underlies the EPYC1–Rubisco condensate. Using biophysical approaches, we found that EPYC1 has five evenly spaced Rubisco-binding regions that share sequence homology and can bind to Rubisco as short peptides. We obtained cryo-electron microscopy structures showing that each of EPYC1's Rubisco-binding regions forms an α -helix that binds one of Rubisco's eight small subunits via salt bridges and hydrophobic interactions. The mapping of these binding sites onto Rubisco holoenzymes in the native pyrenoid matrix indicates that the linker sequences between the Rubisco-binding regions on EPYC1 are sufficiently long to connect adjacent Rubisco holoenzymes. These discoveries advance the understanding of the pyrenoid and provide a high-resolution structural view of a phase-separated organelle.

Results

We could not directly determine the structure of full-length EPYC1 bound to Rubisco because mixing the two proteins together produces phase-separated condensates¹¹. We thus aimed to first identify Rubisco-binding regions on EPYC1 and then use a structural approach to determine how these regions bind to Rubisco.

EPYC1 has five nearly identical Rubisco-binding regions. The intrinsically disordered nature of purified EPYC1 (ref. ¹¹) led us to hypothesize that the Rubisco-binding regions of EPYC1 were

¹Department of Molecular Biology, Princeton University, Princeton, NJ, USA. ²Janelia Research Campus, Howard Hughes Medical Institute, Ashburn, VA, USA. ³Department of Therapeutic Discovery, Amgen Discovery Research, Amgen Inc., South San Francisco, CA, USA. ⁴School of Biological Sciences, Nanyang Technological University, Singapore, Singapore. ⁵SynthSys & Institute of Molecular Plant Sciences, School of Biological Sciences, University of Edinburgh, Edinburgh, UK. ⁶Department of Molecular Structural Biology, Max Planck Institute of Biochemistry, Martinsried, Germany. ⁷Institute of Neuropathology, University of Göttingen Medical Center, Göttingen, Germany. ⁸Department of Biology, Stanford University, Stanford, CA, USA. ⁹Helmholtz Pioneer Campus, Helmholtz Zentrum München, Neuherberg, Germany. ¹⁰Department of Chemistry, Technical University of Munich, Garching, Germany. ✉e-mail: mjonikas@princeton.edu

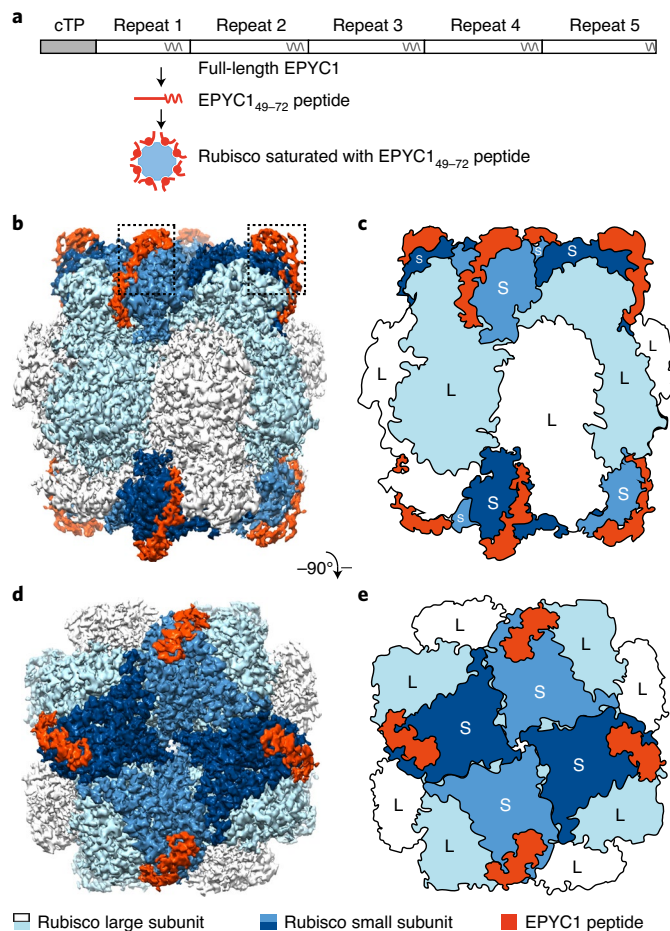


Fig. 2 | EPYC1 binds to Rubisco small subunits. **a**, Peptide EPYC1₄₉₋₇₂, corresponding to the first Rubisco-binding region of EPYC1, was incubated at saturating concentrations with Rubisco prior to single-particle cryo-electron microscopy. **b–e**, Density maps (**b,d**) and cartoons (**c,e**) illustrate the side views (**b,c**) and top views (**d,e**) of the density map of the EPYC1 peptide–Rubisco complex. The dashed boxes in **b** indicate the regions shown in Fig. 3a–f.

EPYC1 repeats leads to a proportional decrease in EPYC1 interaction with Rubisco. It also explains our observation that decreasing the number of EPYC1 repeats leads to a proportional decrease in the tendency of EPYC1 and Rubisco to phase separate together¹¹.

EPYC1 binds to Rubisco small subunits. The sequence homology of the five Rubisco-binding regions suggests that each region binds to Rubisco in a similar manner. To identify the binding site of EPYC1 on Rubisco, we determined three structures by using single-particle cryo-electron microscopy. The first structure consists of Rubisco in complex with peptide EPYC1₄₉₋₇₂, representing the first Rubisco-binding region of EPYC1 (2.13 Å overall resolution; ~2.5 Å EPYC1 peptide local resolution; Fig. 2, Extended Data Figs. 2–5 and Supplementary Table 1). The second structure consists of Rubisco in complex with a second peptide, EPYC1₁₀₆₋₁₃₅, representing the second, third and fourth Rubisco-binding regions of EPYC1 (2.06 Å overall resolution, ~2.5 Å EPYC1 peptide local resolution, Extended Data Fig. 6). The affinities of these peptides to Rubisco were low by protein interaction standards ($K_D \approx 3$ mM; Extended Data Fig. 1d,e); thus, millimolar concentrations of peptide were required to approach full occupancy of peptide bound to Rubisco. For reference purposes, we also obtained a third structure

of Rubisco in the absence of EPYC1 peptide (2.68 Å; Extended Data Figs. 2 and 3), which was nearly identical to the previously published X-ray crystallography structure¹³, with minor differences probably due to the absence of the substrate analogue 2-CABP in the active site of Rubisco in our sample¹⁴ (Extended Data Fig. 4).

The structures of Rubisco in complex with EPYC1₄₉₋₇₂ and of Rubisco in complex with EPYC1₁₀₆₋₁₃₅ were remarkably similar, indicating that these two peptides and the corresponding four regions of EPYC1 each bind to the same site on the Rubisco holoenzyme. The Rubisco holoenzyme consists of a core of eight catalytic large subunits in complex with eight small subunits, four of which cap each end of the holoenzyme (Fig. 2b–e). In each structure, an EPYC1 peptide was clearly visible bound to each Rubisco small subunit, suggesting that each Rubisco holoenzyme can bind up to eight EPYC1s (Fig. 2b–e and Extended Data Fig. 6b,c).

Salt bridges and a hydrophobic interface mediate binding. Both the EPYC1₄₉₋₇₂ and EPYC1₁₀₆₋₁₃₅ peptides formed an extended chain that sits on top of the Rubisco small subunit's two α -helices (Fig. 3a,b and Extended Data Fig. 6d,e). This binding site explains our previous observation that mutations in the Rubisco small subunit α -helices disrupted yeast two-hybrid interactions between EPYC1 and the Rubisco small subunit¹² and prevented Rubisco's assembly into a pyrenoid *in vivo*¹⁵. The C-terminal regions of the EPYC1₄₉₋₇₂ and EPYC1₁₀₆₋₁₃₅ peptides (NW(R/K)QELES(LR(N/S))) are well resolved; each forms an α -helix that runs parallel to helix B of the Rubisco small subunit (Fig. 3a,b). The peptides' N termini extend the trajectory of the helix and follow the surface of the Rubisco small subunit (Figs. 2b–e and 3a,b and Extended Data Figs. 5 and 6b,c). The side chains of the peptides' N termini could not be well resolved, suggesting that these regions are more conformationally flexible.

Our atomic models based on the density maps suggest that binding is mediated by salt bridges and a hydrophobic interface. Three residue pairs of EPYC1₄₉₋₇₂ probably form salt bridges (Fig. 3c,d,g): EPYC1 residues Arg 64 and Arg 71 interact with Glu 24 and Asp 23, respectively, of Rubisco small subunit α -helix A, and EPYC1 residue Glu 66 interacts with Arg 91 of Rubisco small subunit α -helix B. Furthermore, a hydrophobic interface is formed by Trp 63, Leu 67 and Leu 70 of EPYC1 and Met 87, Leu 90 and Val 94 of Rubisco small subunit helix B (Fig. 3e–g). Similar interactions were observed for the corresponding residues in EPYC1₁₀₆₋₁₃₅ (Extended Data Fig. 6f–j).

Binding and phase separation require interface residues. To determine the importance of individual EPYC1 residues for binding, we investigated the impact on Rubisco binding of every possible single amino acid substitution for EPYC1's first Rubisco-binding region by using a peptide array (Fig. 4a and Supplementary Table 4) and SPR (Extended Data Fig. 7). Consistent with our structural model, the peptide array indicated that EPYC1 salt-bridge-forming residues Arg 64, Arg 71 and Glu 66 and the hydrophobic interface residues Trp 63, Leu 67 and Leu 70 were all required for normal EPYC1 binding to Rubisco. The strong agreement of our mutational analysis suggests that our structural model correctly represents EPYC1's Rubisco-binding interface.

To determine the importance of EPYC1's Rubisco-binding regions for pyrenoid matrix formation, we assayed the impacts of mutations in these regions on the formation of phase-separated droplets by EPYC1 and Rubisco *in vitro*. The phase boundary was shifted by mutating Arg 64 in the first Rubisco-binding region and the corresponding Lys or Arg in the other four Rubisco-binding regions of EPYC1 (Fig. 4b and Extended Data Fig. 8), suggesting that the Rubisco-binding regions mediate condensate formation.

Pyrenoid matrix formation requires interface residues. We validated the importance of Rubisco residues for binding to

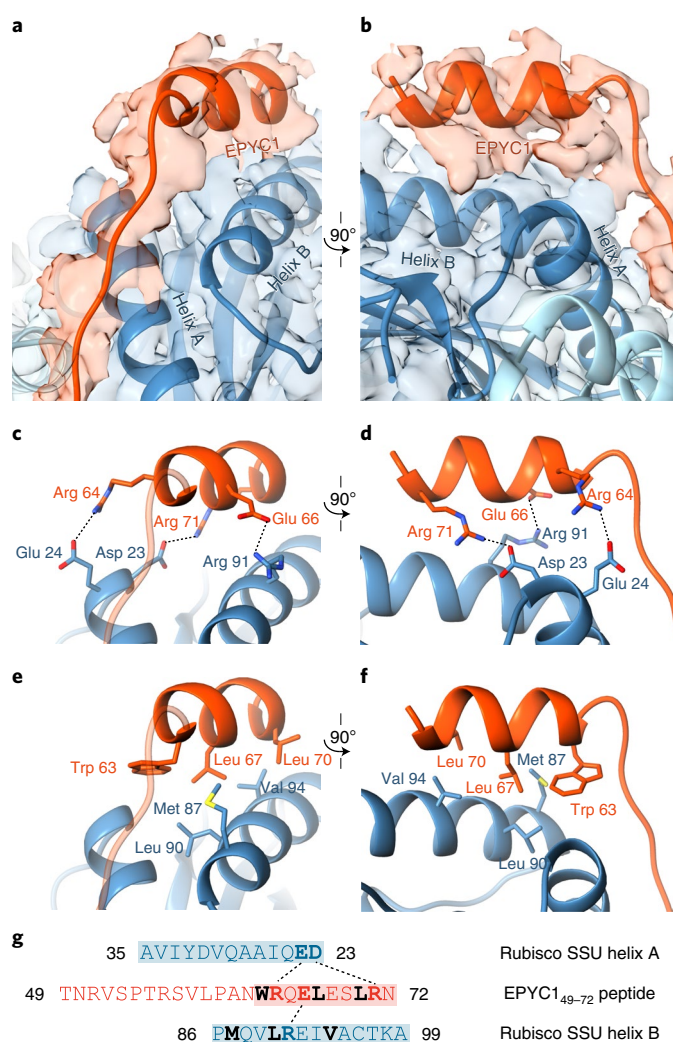


Fig. 3 | EPYC1 binds to Rubisco small subunit α -helices via salt bridges and a hydrophobic pocket. **a, b**, Front (**a**) and side (**b**) views of the EPYC1₄₉₋₇₂ peptide (red) bound to the two α -helices of the Rubisco small subunit (blue). **c, d**, Three pairs of residues form salt bridges between the helix of the EPYC1₄₉₋₇₂ peptide and the helices on the Rubisco small subunit. Shown are front (**c**) and side (**d**) views as in **a** and **b**. The distances from EPYC1 Arg 64, Arg 71 and Glu 66 to Rubisco small subunit Glu 24, Asp 23 and Arg 91 are 3.06 Å, 2.78 Å and 2.79 Å, respectively. **e, f**, A hydrophobic pocket is formed by three residues of the EPYC1₄₉₋₇₂ peptide and three residues of helix B of the Rubisco small subunit. Shown are front (**e**) and side (**f**) views as in **a** and **b**. **g**, Summary of the interactions observed between the EPYC1₄₉₋₇₂ peptide and the two α -helices of the Rubisco small subunit. The helices are highlighted, the residues mediating the interactions are in bold, the salt bridges are shown as dashed lines and the residues contributing to the hydrophobic pocket are shown in black.

EPYC1 by yeast two-hybrid assays (Fig. 5a and Extended Data Fig. 9). A Rubisco small subunit D23A mutation (with Asp23 replaced by Ala23), which eliminates the charge of the aspartate residue, had a severe impact on Rubisco small subunit interaction with EPYC1, as expected from the contribution of that residue to a salt bridge with Arg71 and homologous residues of EPYC1's Rubisco-binding regions. Likewise, E24A and R91A each showed a moderate defect, consistent with the contributions of those residues to salt bridges with Arg64 and Glu66 (and homologous residues) of EPYC1, respectively. Additionally, M87D and V94D, mutations that convert hydrophobic residues to bulky charged residues,

each had a severe impact on interaction, as expected from the participation of those residues in the hydrophobic interface. Combinations of these mutations abolished the interactions completely (Extended Data Fig. 9).

To evaluate the importance of the binding interface in vivo, we generated *C. reinhardtii* strains with point mutations in the binding interface. Rubisco small subunit mutations D23A/E24A or M87D/V94D caused a growth defect under conditions requiring a functional pyrenoid (Fig. 5b and Extended Data Fig. 10a,b). Furthermore, the mutants lacked a visible pyrenoid matrix (Fig. 5c,d and Extended Data Fig. 10c), indicating that those Rubisco small subunit residues are required for matrix formation in vivo. The Rubisco mutants retained pyrenoid tubules¹⁶, as previously observed in other matrix-deficient mutants^{10,17-19}.

Together, our data demonstrate that EPYC1's Rubisco-binding regions bind to the Rubisco small subunit α -helices via salt-bridge interactions and a hydrophobic interface, enabling the condensation of Rubisco into the phase-separated matrix.

A structural model for pyrenoid matrix formation. The presence of multiple Rubisco-binding regions along the EPYC1 sequence supports a model in which consecutive Rubisco-binding regions on the same EPYC1 polypeptide can bind to different Rubisco holoenzymes and thus hold them together to form the pyrenoid matrix. If this model is correct, we would expect that the ~40-amino-acid 'linker' regions between consecutive Rubisco-binding regions on EPYC1 (Fig. 1g,i) would be sufficient to span the distance between EPYC1-binding sites on neighbouring Rubisco holoenzymes in the pyrenoid matrix. To test this aspect of the model, we combined our atomic structure of the EPYC1–Rubisco interaction with the precise positions and orientations of Rubisco holoenzymes within the pyrenoid matrix of native cells that we had previously obtained by in situ cryo-electron tomography⁵ (Fig. 6a,b). We mapped the positions of EPYC1-binding sites onto Rubisco holoenzymes in the matrix and measured the distances between nearest-neighbour EPYC1-binding sites on adjacent holoenzymes (Fig. 6c, binding sites on the same holoenzyme were excluded in this analysis). The observed distances ranged from ~2 nm to ~7 nm, with a median distance of ~4 nm (Fig. 6d and Supplementary Table 5).

A linker region of 40 amino acids is unlikely to be stretched to its maximum possible length of 14 nm in vivo due to the high entropic cost of this configuration. To determine whether a linker region can span the observed distances between nearest-neighbour binding sites on adjacent Rubisco holoenzymes, we used a simple physics model to calculate the energy required to stretch a 40-amino-acid chain to any given distance (Fig. 6d and Methods). The model indicates that stretching the chain to ~7 nm requires an energy of $3k_B T$ (where k_B is the Boltzmann constant and T is the temperature), which could reasonably be derived from thermal fluctuations. Our data thus suggest that the linker region between consecutive Rubisco-binding sites on the EPYC1 polypeptide can span the distance between adjacent Rubisco holoenzymes to hold the pyrenoid matrix together in vivo. It also seems likely that, in addition to bridging neighbouring Rubisco holoenzymes, consecutive Rubisco-binding regions on a given EPYC1 can bind multiple sites on one Rubisco holoenzyme, as the distance between the nearest binding sites on the same holoenzyme is <9 nm.

Discussion

In this study, we have determined the structural basis for matrix formation in a pyrenoid. We found that in the model alga *C. reinhardtii*, the intrinsically disordered protein EPYC1 has five regions of similar sequence that can bind to Rubisco as short peptides. These EPYC1 regions form an α -helix that binds to the Rubisco small subunit α -helices via salt bridges and hydrophobic interactions. EPYC1's Rubisco-binding regions are spaced by linker sequences

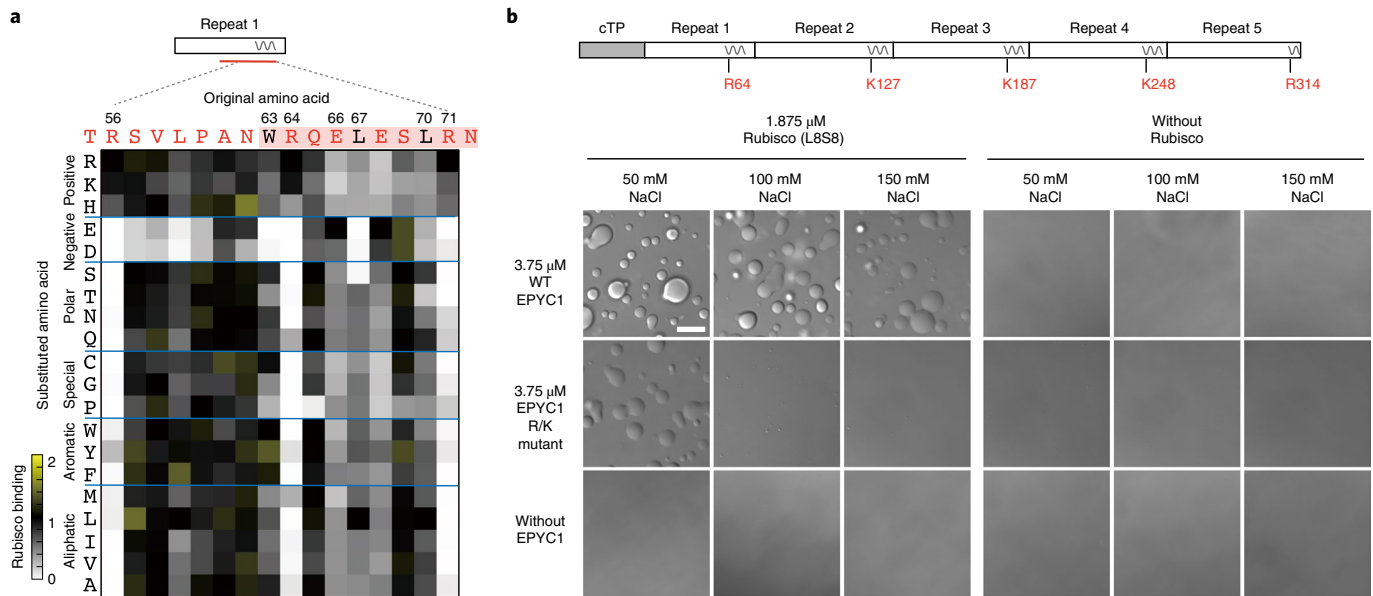


Fig. 4 | Interface residues on EPYC1 are required for the binding and phase separation of EPYC1 and Rubisco in vitro. **a**, Rubisco binding to a peptide array representing every possible single amino acid substitution for amino acids 56–71 of EPYC1. The binding signal was normalized by the binding signal of the original sequence. **b**, The effect of mutating the central Arg or Lys in each of EPYC1's Rubisco-binding regions on the in vitro phase separation of EPYC1 with Rubisco. Scale bar, 10 μ m. For each condition, the experiment was performed twice independently, with similar results.

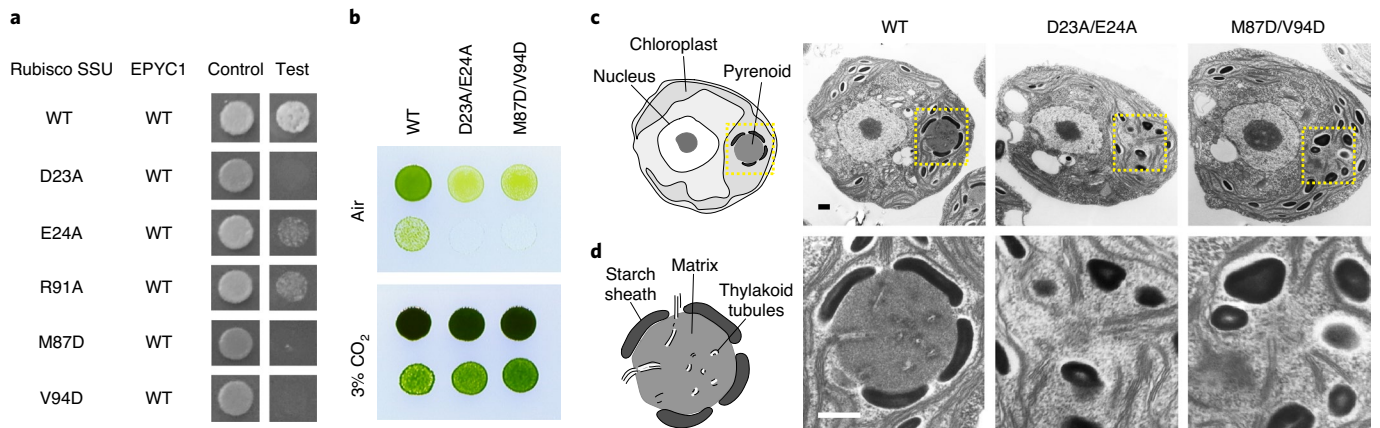


Fig. 5 | Interface residues on Rubisco are required for yeast two-hybrid interactions between EPYC1 and Rubisco and for pyrenoid matrix formation in vivo. **a**, The importance of Rubisco small subunit (SSU) residues for interaction with EPYC1 was tested by mutagenesis in a yeast two-hybrid experiment. **b**, The Rubisco small-subunit-less mutant T60 ($\Delta rbcS$) was transformed with wild-type (WT), D23A/E24A or M87D/V94D Rubisco small subunits. Serial 1:10 dilutions of cell cultures were spotted on TP minimal medium and grown in air or 3% CO₂. **c,d**, Representative electron micrographs of whole cells (**c**) and corresponding pyrenoids (**d**) of the strains expressing WT, D23A/E24A and M87D/V94D Rubisco small subunit. The dashed lines in **c** indicate the regions shown in **d**. Scale bars, 500 nm. At least 25 cells were imaged for each strain; additional representative images are shown in Extended Data Fig. 10c.

that are sufficiently long to span the distance between binding sites on adjacent Rubisco holoenzymes within the pyrenoid, allowing EPYC1 to serve as a molecular glue that clusters Rubisco together to form the pyrenoid matrix (Fig. 6e).

The multivalency of EPYC1 and the high K_D (~ 3 mM; Extended Data Fig. 1e) of individual Rubisco-binding regions are consistent with the emerging principle that cellular phase separation is mediated by weak multivalent interactions²⁰. The high dissociation rate constant (>1 s⁻¹; Extended Data Fig. 1d) of individual Rubisco-binding regions explains how the pyrenoid matrix can mix internally on the timescale of seconds⁵ despite the multivalency of EPYC1. The even spacing of the five Rubisco-binding regions across

EPYC1 is noteworthy and may be an indication of selective pressure for an optimal distance between binding regions, and thus of an optimal spacing between Rubisco holoenzymes in the matrix.

Knowledge of the EPYC1–Rubisco binding mechanism opens doors to the molecular characterization of the regulation of this interaction, which may govern the dissolution and condensation of the matrix during cell division⁵ and in response to environmental factors²¹. For example, the phosphorylation of EPYC1 (ref. 22) may provide a mechanism to rapidly change the binding affinity of EPYC1 to Rubisco. The inactivation of one Rubisco-binding region on EPYC1 would yield four binding regions, which would allow two such EPYC1 molecules (each containing four Rubisco-binding

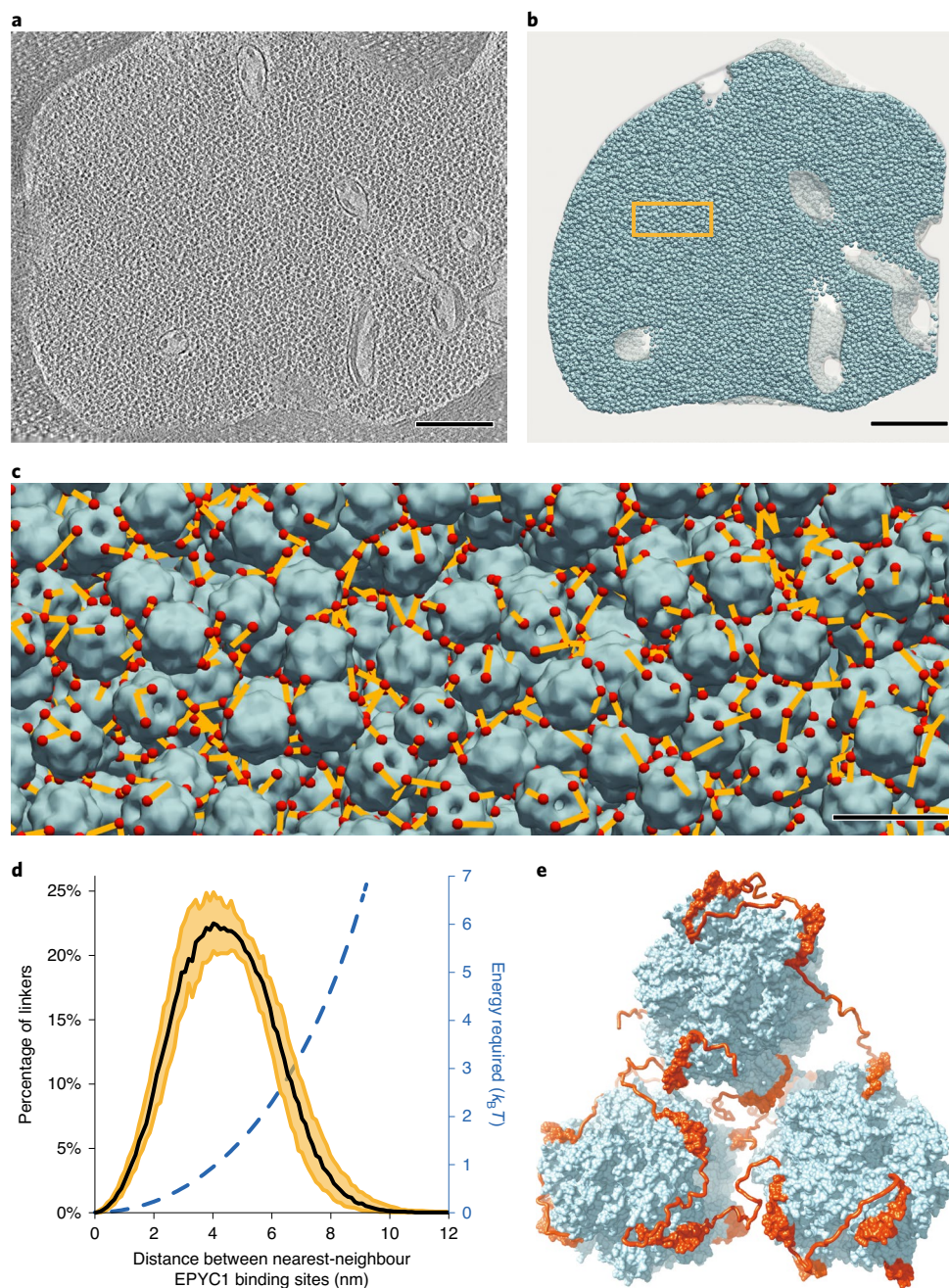


Fig. 6 | A model for matrix structure consistent with in situ Rubisco positions and orientations. **a**, The pyrenoid matrix was imaged by cryo-electron tomography⁵. An individual slice through the three-dimensional volume is shown. Scale bar, 200 nm. **b**, The positions and orientations of individual Rubisco holoenzymes (blue) were determined with high sensitivity and specificity (97.5% positive identification) by template matching, subtomogram averaging and classification and were then mapped back into the tomogram volume shown in **a**. The yellow box indicates the region shown in **c**. Scale bar, 200 nm. **c**, The distances (yellow) between the nearest EPYC1-binding sites (red) on neighbouring Rubisco holoenzymes (blue) were measured. The view is from inside the matrix; in some cases, the nearest EPYC1-binding site is on a Rubisco that is out of the field of view, causing some yellow lines to appear unconnected in this image. Scale bar, 20 nm. The data shown in **a–c** are representative of the five independent tomograms used for this study. **d**, Histogram showing the distances between the nearest EPYC1-binding sites on neighbouring Rubisco holoenzymes. The black line indicates the median, and the yellow shading indicates the 95% confidence interval based on data from five independent tomograms. The estimated energy required for stretching a chain of 40 amino acids a given distance is shown in blue. **e**, A three-dimensional model illustrates how EPYC1 (red) could crosslink multiple Rubisco holoenzymes (blue) to form the pyrenoid matrix. The conformations of the intrinsically disordered linkers between EPYC1-binding sites were modelled hypothetically.

regions, for a total of eight Rubisco-binding regions) to form a mutually satisfied complex with each Rubisco holoenzyme (containing eight EPYC1-binding sites), a configuration that is predicted to favour the dissolution of the matrix⁵.

Binding of other pyrenoid proteins to Rubisco. In a parallel study²³, we recently discovered that a common sequence motif is present on many pyrenoid-localized proteins. The motif binds Rubisco, enabling the recruitment of motif-containing proteins to the

pyrenoid and mediating adhesion between the matrix, pyrenoid tubules and starch sheath. This motif, (Asp/Asn)Trp(Arg/Lys)XX(Leu/Ile/Val/Ala), is present in EPYC1's Rubisco-binding regions as defined in the present study, and the motif residues mediate key binding interactions with Rubisco. In our structures, the Arg/Lys of the motif is represented by Arg64 and Lys127 of EPYC1, each of which forms a salt bridge with Glu24 of the Rubisco small subunit. The XX of the motif almost always includes an Asp or Glu; in our structures, this feature is represented by Glu66 and Glu129 of EPYC1, each of which forms a salt bridge with Arg91 of the Rubisco small subunit. Finally, the Trp and Leu/Ile/Val/Ala of the motif are represented by Trp63/Trp126 and Leu67/Leu130 of EPYC1, which contribute to the hydrophobic interactions with Met87, Leu90 and Val94 of the Rubisco small subunit. The key roles of the motif residues in the interface presented here strongly suggest that the structures we have obtained for motifs from EPYC1 also explain where and how all other variants of the motif (including those found on the key pyrenoid proteins SAGA1, SAGA2, RBMP1, RBMP2 and CSP41A) bind to Rubisco. Our observation that the Rubisco small subunit D23A/E24A and M87D/V94D mutants exhibit a more severe disruption of the pyrenoid than the *epyc1* mutant¹⁰ supports the idea that this region of Rubisco interacts not only with EPYC1 but also with other proteins required for pyrenoid biogenesis, making this binding interaction a central hub of pyrenoid biogenesis.

Structural differences between the pyrenoid and carboxysomes.

Although α - and β -carboxysomes are morphologically, functionally and evolutionarily distinct from the pyrenoid, their Rubisco is also thought to be clustered by linker proteins. Like EPYC1, the α -carboxysome linker protein CsoS2 (ref. ²⁴) is intrinsically disordered and is proposed to bind Rubisco as an unfolded peptide²⁵. In contrast, the β -carboxysome linker protein CcmM has been proposed to bind Rubisco using folded globular domains^{26,27}. The use of an unfolded peptide as in the case of EPYC1 and CsoS2 may provide the benefit of requiring fewer amino acids for achieving the desired binding function. A notable difference is the location of the binding site on Rubisco: whereas both carboxysomal linker proteins bind to the interface between two Rubisco large subunits^{25,27}, EPYC1 binds to the Rubisco small subunit. It remains to be seen whether this difference in binding site has functional consequences, such as impacts on the three-dimensional packing of Rubisco.

Ability to engineer a pyrenoid. There is currently substantial interest in engineering Rubisco condensates into monocotyledonous crops such as wheat and rice to enhance yields^{28–31}. The binding of EPYC1 to the Rubisco small subunit presents a promising route for engineering a Rubisco condensate, as the Rubisco small subunit is encoded in the nuclear genome, making it more easily amenable to genetic modification in those crops than the chloroplast-encoded Rubisco large subunit³². Knowledge of the binding mechanism allows the engineering of minimal sequence changes into native crop Rubiscos to enable binding to EPYC1 and to other key proteins required to reconstitute a functional pyrenoid.

Insights into pyrenoid matrix formation in other species.

Pyrenoids seem to have evolved independently in different lineages through convergent evolution^{7,33}. EPYC1, its Rubisco-binding sequences and the amino acid residues that form the EPYC1-binding site on the surface of Rubisco are conserved across the order Volvocales, as evidenced from the genome sequences of *Tetrabaena socialis*, *Gonium pectorale* and *Volvox carteri* (Supplementary Table 2). While the molecular mechanisms of matrix formation in other lineages remain to be uncovered, candidate linker proteins have been identified on the basis of similarity of sequence properties to EPYC1 (ref. ¹⁰). We hypothesize that the matrix in other lineages is formed on the basis of similar principles to those we observed

in *C. reinhardtii*. Our experimental approach for characterizing the binding interaction provides a road map for future structural studies of pyrenoids across the tree of life.

Structural view of a phase-separated organelle. The pyrenoid matrix presents an unusual opportunity to study a two-component molecular condensate where one of the components, Rubisco, is large and rigid, and the other component, EPYC1, is a simple intrinsically disordered protein consisting of nearly identical tandem repeats. The rigidity and size of Rubisco holoenzymes previously enabled the determination of their positions and orientations within the pyrenoid matrix of native cells by cryo-electron tomography⁵. The identification of EPYC1-binding sites on Rubisco in the present work and the modelling of linker regions between EPYC1's Rubisco-binding regions now make the *C. reinhardtii* pyrenoid matrix one of the most structurally well-defined phase-separated organelles. Thus, beyond advancing our structural understanding of pyrenoids (organelles that play a central role in the global carbon cycle), we hope that the findings presented here will also more broadly enable advances in the biophysical understanding of phase-separated organelles.

Methods

Strains and culture conditions. *C. reinhardtii* WT strain cMJ030 was maintained in the dark or low light ($\sim 10 \mu\text{mol photons per m}^2 \text{ per second}$) on 1.5% agar plates containing Tris-acetate-phosphate medium with revised trace elements³⁴. For Rubisco extraction, 500 ml of Tris-acetate-phosphate medium in a 1 l flask was inoculated with a loopful of cells, and the culture was grown to 4×10^6 cells per ml at 22 °C, shaking at 200 r.p.m. under $\sim 100 \mu\text{mol photons per m}^2 \text{ per second}$ white light in 3% CO₂. *C. reinhardtii* mutant T60-3 (ref. ³⁵) ($\Delta rbcS$; containing a deletion of both *RBCS* genes) was used for generating Rubisco small subunit point mutants and a WT control in the same background. This strain was maintained on agar in the dark or low light ($\sim 10 \mu\text{mol photons per m}^2 \text{ per second}$).

Protein extraction. Rubisco was purified from *C. reinhardtii* strain cMJ030 (ref. ³⁶). The cells were disrupted by ultrasonication in lysis buffer (10 mM MgCl₂, 50 mM Bicine, 10 mM NaHCO₃, 1 mM dithiothreitol, pH 8.0) supplemented with Halt Protease Inhibitor Cocktail, EDTA-Free (Thermo Fisher Scientific). The soluble lysate was fractionated by ultracentrifugation on a 10–30% sucrose gradient in a SW 41 Ti rotor at a speed of 35,000 r.p.m. for 20 hours at 4 °C. Rubisco-containing fractions were applied to an anion exchange column (MONO Q 5/50 GL, GE Healthcare) and eluted with a linear salt gradient from 30 to 500 mM NaCl in lysis buffer.

Peptide arrays. The peptide arrays were purchased from the MIT Biopolymers Laboratory. The tiling array was composed of 18-amino-acid peptides that tiled across the full-length EPYC1 sequence with a step size of one amino acid. Each peptide was represented by at least two spots on the array, and these replicates were averaged during data analysis. The locations of peptides on the array were randomized. In the substitution arrays, peptides were designed to represent every possible one-amino-acid mutation of the indicated region on EPYC1 by substitution with one of the other 19 amino acids. The arrays were activated by methanol and then washed $3 \times 10 \text{ min}$ in binding buffer (50 mM HEPES, 50 mM KOAc, 2 mM Mg(OAc)₂·4H₂O, 1 mM CaCl₂, and 200 mM sorbitol, pH 6.8). The arrays were then incubated at 4 °C with 1 mg purified Rubisco overnight. The arrays were washed in binding buffer to remove any unbound Rubisco. Using a semi-dry transfer apparatus (BIO-RAD), bound Rubisco was transferred onto an Immobilon-P PVDF membrane (Millipore Sigma). The Rubisco was detected by one of two methods: western blotting or fluorescent labelling. While replicates using the two methods gave similar results, toward the end of the project we found that fluorescent labelling had a lower background, so we show the fluorescent labelling data in Fig. 1; all other data were obtained by western blotting and chemiluminescence. For fluorescent labelling, Rubisco was labelled with Alexa Fluor 680 dye (Thermo Fisher Scientific) and detected by Typhoon Scanner (GE Healthcare). For western blotting, Rubisco was immuno-detected with a polyclonal primary antibody raised against Rubisco¹⁵ (1:10,000) followed by a HRP conjugated goat anti-rabbit (1:20,000; Invitrogen), and the chemiluminescence was detected by ImageQuant LAS 4000 (GE Healthcare). The images were analysed with ImageQuant TL (GE Healthcare). The arrays were stripped with RestoreWestern Blot Stripping Buffer before reuse (Thermo Fisher Scientific).

For both types of arrays, the values for identical sequences present multiple times were averaged. For the tiling arrays, the average value for each sequence was plotted at its position in EPYC1 (or at multiple positions for sequences present multiple times). For the amino acid substitution arrays, the ratio of each

substitution sequence to the corresponding WT sequence was calculated and arrayed by amino acid and position.

Surface plasmon resonance experiments. All the surface preparation experiments were performed at 25 °C using a Biacore 3000 instrument (GE Healthcare). Purified Rubisco was immobilized on CM5 sensor chips using a Biacore Amine Coupling Kit according to the manufacturer's instructions. Briefly, the chip surface was activated by an injection of 1:1 N-hydroxysuccinimide/1-ethyl-3-(3-dimethylaminopropyl)carbodiimide hydrochloride. Rubisco was diluted to ~100 µg ml⁻¹ in 10 mM acetate (pH 4.5; this pH had been previously optimized using the immobilization pH scouting wizard) and was injected over the chip surface. Excess free amine groups were then capped with an injection of 1 M ethanolamine. The typical immobilization levels were 8,000 to 10,000 resonance units, as recommended for binding experiments of small molecules. For the kinetic experiments (for determining the binding affinities), the typical immobilization levels were ~5,000 resonance units. The control surfaces were prepared in exactly the same manner as the experimental surfaces except that no Rubisco was injected. For the immobilizations, the running buffer was the Biacore HBS-EP Buffer (0.01 M HEPES pH 7.4, 0.15 M NaCl, 3 mM EDTA, 0.005% v/v Surfactant P20).

All the binding assays were performed using the Biacore PBS-P + Buffer (20 mM phosphate buffer, 2.7 mM KCl, 137 mM NaCl and 0.05% Surfactant P20, pH 6.8) as a running buffer, as recommended for small molecule analysis in Biacore systems. The analytes, consisting of EPYC1 peptides synthesized by Genscript, were dissolved in the same running buffer and diluted to 1 mM. The analytes were injected over the control surface and experimental surfaces at a flow rate of 26 µl min⁻¹ for 2.5 min, followed by 2.5 min of the running buffer alone to allow for dissociation. The surfaces were then regenerated using the running buffer at a flow rate of 30 µl min⁻¹ for 10 min. In all cases, binding to the control surface was negligible.

For determining the K_D of EPYC1 peptide, the kinetic assays were performed with a running buffer consisting of 200 mM sorbitol, 50 mM HEPES, 50 mM KOAc, 2 mM Mg(OAc)₂·4H₂O and 1 mM CaCl₂ at pH 6.8 (the same buffer as the peptide array assay). The EPYC1 peptide was dissolved in the same running buffer as the assay, and the serial dilutions were also made in the same buffer. The analytes were injected over the control surface and experimental surfaces at a flow rate of 15 µl min⁻¹ for 2 min, followed by 10 min with the running buffer alone to allow for dissociation. The surfaces were then regenerated by the running buffer at a flow rate of 30 µl min⁻¹ for 10 min. In all cases, binding to the blank chip was negligible. The fitting and modelling were performed with the BIAevaluation software³⁷.

Single-particle cryo-electron microscopy data collection and image processing.

Rubisco and EPYC1₄₉₋₇₂ peptides with the final concentrations of 1.69 mg ml⁻¹ (3.02 µM) and 7.5 mM, respectively, were incubated together on ice for 20 minutes in buffer consisting of 200 mM sorbitol, 50 mM HEPES, 50 mM KOAc, 2 mM Mg(OAc)₂·4H₂O and 1 mM CaCl₂ at pH 6.8 (the same buffer as the peptide array assay and the SPR binding assay). Rubisco and EPYC1₁₀₆₋₁₃₅ peptides with the final concentrations of 1.75 mg ml⁻¹ (3.13 µM) and 10 mM, respectively, were incubated together on ice for 20 minutes in the same buffer described above. For apo Rubisco and Rubisco incubated with peptides, similar cryo-grid-making procedures were used. 400-mesh Quantifoil 1.2/1.3 Cu grids (Quantifoil) were made hydrophilic by glow discharging for 60 seconds with a current of 15 mA in a PELCO easiGlow system. The cryo grids were produced using a FEI Mark IV Vitrobot (FEI Company, part of Thermo Fisher Scientific). The chamber of the Vitrobot was kept at 4 °C and 100% relative humidity. 3 µl of sample was applied to the glow-discharged grid and blotted with filter paper for 3 seconds with the equipment-specific blotting force set at 3. After blotting, the grid was rapidly plunge-frozen into a liquid ethane bath.

For apo Rubisco and Rubisco incubated with EPYC1₄₉₋₇₂ peptide, the cryo grids were loaded into a 300 kV FEI Titan Krios cryo electron microscope (FEI Company) at HHMI Janelia Research Campus, Janelia Krios2, equipped with a Gatan K2 Summit camera. After the initial screening and evaluation, fully automated data collection was carried out using SerialEM. The final exposure from each collection target was collected as a video using dose fractionation on the K2 Summit camera operated in super-resolution mode. The videos were collected at a calibrated magnification of ×38,168, corresponding to 1.31 Å per physical pixel in the image (0.655 Å per super-resolution pixel). The dose rate on the specimen was set to be 5.82 electrons per Å² per second, and the total exposure time was 10 s, resulting in a total dose of 58.2 electrons per Å². With the dose fractionation set at 0.2 s per frame, each video series contained 50 frames, and each frame received a dose of 1.16 electrons per Å². The spherical aberration constant of the objective lens is 2.7 mm, and an objective aperture of 100 µm was used. The nominal defocus range for the automated data collection was set to be between -1.5 µm and -3.0 µm. For Rubisco incubated with EPYC1₁₀₆₋₁₃₅ peptide, the final exposure was collected on Janelia Krios1 equipped with a C_s-corrector, a Gatan Bioquantum energy filter and a post-filter K3 camera. The videos were collected at a nominal magnification of ×81,000, corresponding to 0.844 Å per physical pixel in the image (0.422 Å per super-resolution pixel). The dose rate on the specimen was set to be 12 electrons per pixel per second, and the total exposure time was 3.56 s, resulting in a total dose of 60 electrons per Å². Each video series contained 60 frames, and

each frame received a dose of 1 electron per Å². The nominal defocus range for the automated data collection was set to be between -1 µm and -1.6 µm.

The videos were 2× binned and motion corrected using MotionCor2 (ref. 38), and CTF was estimated using CTFIND³⁹ in Relion⁴⁰. In total, 1,809,869 EPYC1₄₉₋₇₂ peptide-bound Rubisco particles, 2,257,131 EPYC1₁₀₆₋₁₃₅ peptide-bound Rubisco particles and 677,071 Rubisco particles in the apo state were selected using cisTEM⁴¹. Two-dimensional classification was performed using cisTEM. The classes presenting detailed features in class averages were chosen for three-dimensional classification on cryoSPARC^{42,43} and on Relion. The three-dimensional class showing clear secondary structures was chosen for three-dimensional auto-refine, first without symmetry and then with D4 symmetry imposed. After CTF refinement and Bayesian polishing in Relion, the reconstructed map resolution is 2.68 Å for the apo state, 2.62 Å for the EPYC1₄₉₋₇₂ peptide-bound state and 2.06 Å for the EPYC1₁₀₆₋₁₃₅ peptide-bound state. The EPYC1₄₉₋₇₂ peptide-bound particles at super-resolution pixel size were further subjected to CTF refinement and polishing, resulting in map at 2.13 Å resolution. The details for the single-particle cryo-electron microscopy data collection and image processing are included in Supplementary Table 1.

Single-particle cryo-electron microscopy model building, fitting and refinement.

A full model for Rubisco from *C. reinhardtii* was produced from an X-ray structure¹³ (PDB entry 1GK8) and used for rigid body fitting into a local resolution filtered apo or EPYC1₄₉₋₇₂ peptide-bound Rubisco cryo-electron microscopy map using UCSF Chimera⁴⁴. After rigid body fitting of the full complex, initial flexible fitting was performed in COOT⁴⁵ by manually going through the entire peptide chain of a single large and small Rubisco subunit before applying the changes to the other seven large and small subunits. The C-terminal part of the small subunit was built manually, and the sequences were updated to the RBCS2 sequences. The sequence of the EPYC1₄₉₋₇₂ peptide was used to predict secondary structure elements using JPred4 (ref. 46), which gave the prediction that the C-terminal region (NWRQELES) is α-helical. Guided by this prediction, the peptide was built manually into the density using COOT. Additional maps (such as the initial 2.62 Å from the binned data and maps filtered to different resolutions with various applied B-factors) were also used to help with model building in unclear regions. Additional real space refinement of the entire complex was performed using Phenix⁴⁷. The EPYC1₁₀₆₋₁₃₅ peptide-bound map was used to build a model of the EPYC1₁₀₆₋₁₃₅ peptide. First, rigid body fitting of the EPYC1₄₉₋₇₂ peptide-bound Rubisco model into a local resolution filtered EPYC1₁₀₆₋₁₃₅ peptide-bound Rubisco cryo-electron microscopy map was performed using UCSF Chimera. Then, the sequence of the peptide was mutated to the EPYC1₁₀₆₋₁₃₅ peptide sequence, followed by flexible fitting to slightly adjust the PDB to the density. The models were subjected to an all-atom structure validation using MolProbity⁴⁸. The figures were produced using UCSF Chimera.

Liquid-liquid phase separation assay. Proteins used in the liquid-liquid phase separation assay were obtained and stored essentially as described previously⁴¹. Briefly, Rubisco was purified from *C. reinhardtii* cells (CC-2677 cw15 nit1-305 mt-5D, Chlamydomonas Resource Center), grown in Sueoka's high-salt medium⁴⁹, using a combination of anion exchange chromatography and gel filtration.

The EPYC1 full-length gene (encoding amino acids 1-317) and the corresponding Arg/Lys mutant (EPYC1^{R64A/K127A/K187A/K248A/R314A}) were synthesized by GenScript and cloned between the SacII and HindIII site of the pHue vector⁵⁰. The proteins were produced in the *E. coli* strain BL21 (DE3) harbouring pBADES1⁵¹ for coexpression of the *E. coli* chaperonin GroEL/S. The purification was conducted with minor changes (dialysis for the removal of high imidazol concentrations was skipped by running the gel-filtration column before the second IMAC). After the first IMAC step and cleavage⁵² of the N-terminal His₆-ubiquitin tag, the proteins were separated by gel filtration. Finally, the peak fraction was passed a second time through an IMAC column, collecting EPYC1 from the flow through.

The EPYC1-Rubisco condensates were reconstituted in vitro in a buffer containing 20 mM Tris-HCl (pH 8.0) and NaCl concentrations as indicated. 5 µl reactions were incubated for three minutes at room temperature before monitoring the droplet formation by differential interference contrast (DIC) microscopy. The DIC images were acquired with a Nikon Eclipse Ti Inverted Microscope using a ×60 oil-immersion objective after allowing the droplets to settle on the coverslip (Superior Marienfeld) surface for about three minutes. For the droplet sedimentation assays, 10 µl reactions were incubated for three minutes at 20 °C before separating the droplets from the bulk phase by spinning for three minutes at 21,000 g and 4 °C. The pelleted droplets and supernatant fractions were analysed using Coomassie-stained SDS-PAGE.

Yeast two-hybrid assay. Yeast two-hybrid to detect interactions between EPYC1 and RbcS1 was carried out as described previously¹². EPYC1 was cloned into the two-hybrid vector pGBKT7 to create a fusion with the GAL4 DNA-binding domain. Point mutations were introduced by PCR into RbcS1, which was then cloned in the pGADT7 to create a fusion with the GAL4 activation domain. Yeast cells were then cotransformed with binding and activation domain vectors. Successful transformants were cultured, diluted to an optical density at 600 nm (OD₆₀₀) of 0.5 or 0.1 and plated onto SD-L-W and SD-L-W-H containing

increasing concentrations of the HIS3 inhibitor triaminotriazole (3-AT). The plates were imaged after three days. The spots shown in Fig. 5a were grown at 5 mM 3-AT from a starting OD₆₀₀ of 0.5; they are a subset of the full dataset shown in Extended Data Fig. 6.

Cloning of Rubisco small subunit point mutants. The plasmid pSS1-ITP (ref. 53), which contains *C. reinhardtii* *RBCS1* including untranslated regions and introns 1 and 2, was used as a starting point for generating plasmids pSH001 and pSH002, which encode *RBCS1*^{D23A/E24A} and *RBCS1*^{M87D/V94D}, respectively. The point mutations were generated by Gibson assembly⁵⁴ of gBlocks (synthesized by Integrated DNA Technologies) containing the desired mutations into pSS-ITP that had been enzyme digested by restriction endonucleases (XcmI and BbvCI for the D23A/E24A mutations and BbvCI and BspI for the M87D/V94D mutations). All constructs were verified by Sanger sequencing.

The fragment for making pSH001 (containing the D23A/E24A Rubisco small subunit mutant) had the following sequence:

GCAGGGCTGCCCGGCTCAGCCAACAGATGATGGTCTGGACCC
CGGTCAACAACAAGATGTCGAGACCTTCTCTACTGCCTCTCTGAC
CGCCGCAGATCGCCGCCAGGTCGACTACATCGTGCACAACGGTGGGA
TCCCTGCCTGGAGTTCGCTGAGGCCGACAAGGCCTACGTGTCCAAC

The fragment for making pSH002 (containing the M87D/V94D Rubisco small subunit mutant) had the following sequence:

CTGCTGGAGTTCGCTGAGGCCGACAAGGCCTACGTGTCCAACGAG
TCGGCCATCCGCTTCGGCAGCGTGTCTTGCCTGTACTAGACAACCGCT
ACTGCACCATGTGGAAGTGCCTACATGTTTCGGCTGCCGCGACCCCGACCA
GGTGTCTGGCGAGATCGACTGCCTGCACCAAGGCCTTCCCGATGCCTAC
GTGGCCTGGTGGCTTCGACAACGAGAAGCAGGTGCAGATCATGGGC
TTCCTGGTCCAGCCCAAGACTGCCCGGACTTCCAGCCCGCAACA
AGCGCTCCGTGTAATGGAGGCGCTCGTGCATCTGAGCCGTGTGTGATG
TTTGTGGTGTGGTGGAGCGAGTGCATGAGAGTGTGTGTGTGTGTGTGT
TGGTGTGTGGCTAAGCCAAGCGTGTGATCGC

Both the plasmids pSH001 and pSH002 have been submitted to the Chlamydomonas Resource Center (www.chlamycollection.org).

Transformation of *C. reinhardtii* to make the Rubisco small subunit point mutants. *C. reinhardtii* strains $\Delta rbcS$; *RBCS*^{WT}, $\Delta rbcS$; *RBCS*^{D23A/E24A} and $\Delta rbcS$; *RBCS*^{M87D/V94D} (the accession numbers of these strains in the Chlamydomonas Resource Center are CC-5616, CC-5617 and CC-5618, respectively) were generated by transforming pSS1-ITP, pSH001 and pSH002 (encoding Rubisco small subunit constructs) into the Rubisco small subunit deletion mutant T60 ($\Delta rbcS$) by electroporation as described previously⁵⁵. For each transformation, 29 ng kb⁻¹ of KpnI linearized plasmid was mixed with 250 μ l of 2×10^8 cells per ml at 16 °C and electroporated immediately. Transformant colonies were selected on Tris-phosphate plates without antibiotics at 3% v/v CO₂ under ~50 μ mol photons per m² per second light. The sequence of *RbcS* in the transformants was verified by PCR amplification and Sanger sequencing.

Spot tests. For the spot tests, $\Delta rbcS$; *RBCS*^{WT}, $\Delta rbcS$; *RBCS*^{D23A/E24A} and $\Delta rbcS$; *RBCS*^{M87D/V94D} were grown in Tris-phosphate medium at 3% CO₂ until ~ 2×10^7 cells per ml. The cells were diluted in Tris-phosphate medium to a concentration of 8.7×10^7 cells per ml and then serially diluted 1:10 three times. 7.5 μ l of each dilution was spotted onto four TP plates and incubated in air or 3% CO₂ under 20 or 100 μ mol photons per m² per second white light for nine days before imaging.

Transmission electron microscopy. The samples for electron microscopy were fixed for one hour at room temperature in 2.5% glutaraldehyde in Tris-phosphate medium (pH 7.4), followed by one hour at room temperature in 1% OsO₄, 1.5% K₂Fe(CN)₆ and 2 mM CaCl₂. The fixed cells were then bulk stained for one hour in 2% uranyl acetate and 0.05 M maleate buffer at pH 5.5. After serial dehydration (50%, 75%, 95% and 100% ethanol, followed by 100% acetonitrile), the samples were embedded in epoxy resin containing 34% Quetol 651, 44% nonenyl succinic anhydride, 20% methyl-5-norbornene-2,3-dicarboxylic anhydride and 2% catalyst dimethylbenzylamine. Ultramicrotomy was done by the Core Imaging Lab, Medical School, Rutgers University. Imaging was performed at the Imaging and Analysis Center, Princeton University, on a CM100 transmission electron microscope (Philips) at 80 kV.

Measurement of nearest-neighbour distances between EPYC1-binding sites on Rubisco holoenzymes within pyrenoids. See our previous study⁵ for detailed descriptions of the *C. reinhardtii* cell culture, the vitrification of cells onto EM grids, the thinning of cells by cryo-focused ion beam milling, the three-dimensional imaging of native pyrenoids by cryo-electron tomography, tomographic reconstruction, template matching and subtomogram averaging. In that study, we measured the distances between the centre positions of Rubisco complexes within tomograms of five pyrenoids. The spatial parameters determined in that study were combined with the EPYC1-binding sites resolved here by cryo-electron microscopy single-particle analysis to measure the nearest-neighbour distances between EPYC1-binding sites on adjacent Rubisco complexes in the native pyrenoid matrix.

The in situ subtomogram average EMD-3694 (ref. 5) was used as the reference for the Rubisco model. We extracted the isosurface from this density using the 0.5 contour level recommended in the Electron Microscopy Data Bank entry. We then fit the atomic model of EPYC1-bound Rubisco (Fig. 2) within the EMD-3694 density, and for each EPYC1-binding site, we marked the closest point on the isosurface to define the EPYC1-binding sites on this model. The positions and orientations previously determined by subtomogram averaging were used to place each Rubisco model and its corresponding binding sites into the pyrenoid tomograms using the PySeg program⁵⁶.

To compute the nearest-neighbour distances between EPYC1-binding sites on two different Rubisco complexes, first, linkers were drawn between each EPYC1-binding site and all other binding sites within 25 nm. Binding sites on the same Rubisco complex were ignored. Next, the linkers were filtered by length (defined as the Euclidean distance between the two binding sites), and only the shortest linker was retained for each binding site. To prevent edge effects, linkers were discarded if they had a binding site <12 nm from the masked excluded volume (grey in Fig. 6b), which marks the border of the analysed pyrenoid matrix. Finally, the linker distances were plotted in a histogram to show the distribution of lengths (normalized to 100%).

Regarding the accuracy of the Rubisco localization in the previous study⁵, we used template matching, subtomogram alignment and hierarchical classification to identify 97.5% of the Rubisco complexes in each of the five pyrenoid volumes. The Rubisco average was determined at a resolution of 16.5 Å. This could be interpreted to mean that the Rubisco complexes were localized with 1.65 nm precision. However, this resolution is not a simple reflection of translational and rotational accuracy; it is also greatly limited by the contrast transfer function and pixel size of the tomographic data. Furthermore, with this localization uncertainty being random for each particle, it would not change the ~4 nm peak distance between neighbouring EPYC1-binding sites measured in our current study.

Modelling of the energy required to stretch EPYC1 linker regions. The energy required to stretch the linker regions between EPYC1's Rubisco-binding regions was determined as follows. The force F required to stretch a 40-amino-acid linker region to any given length z was approximated using a wormlike chain model⁵⁷:

$$F(z) = \frac{k_B T}{4L_p} \left[\frac{1}{(1 - z/L_0)^2} - 1 + \frac{4z}{L_0} \right]$$

In the above equation, k_B is the Boltzmann constant, T is the temperature, L_p is the persistence length (assumed to be 1 nm, a representative value for disordered proteins) and L_0 is the contour length (estimated as 40 amino acids \times 0.36 nm per amino acid). The energy required to stretch the linker to a length x is given by:

$$E(x) = \int_0^x F(z) dz$$

This energy was calculated and plotted in Fig. 6d.

Reporting Summary. Further information on research design is available in the Nature Research Reporting Summary linked to this article.

Data availability

All data generated or analysed during this study are included in this Article, the extended data and the supplementary tables. The single-particle cryo-electron microscopy maps have been deposited in the Electron Microscopy Data Bank with accession codes EMD-22401, EMD-22308 and EMD-22462. The atomic models have been deposited in the Protein Data Bank under accession codes PDB 7JN4, PDB 7JFO and PDB 7JSX. The raw datasets have been deposited in the Electron Microscopy Public Image Archive with accession codes EMPIAR-10503, EMPIAR-10502 and EMPIAR-10501. The subtomogram average of Rubisco has been deposited in the Electron Microscopy Data Bank with accession code EMD-3694.

Received: 1 June 2020; Accepted: 21 October 2020;
Published online: 23 November 2020

References

- Field, C. B., Behrenfeld, M. J., Randerson, J. T. & Falkowski, P. Primary production of the biosphere: integrating terrestrial and oceanic components. *Science* **281**, 237–240 (1998).
- Hessler, A. M., Lowe, D. R., Jones, R. L. & Bird, D. K. A lower limit for atmospheric carbon dioxide levels 3.2 billion years ago. *Nature* **428**, 736–738 (2004).
- Ainsworth, E. A. & Long, S. P. What have we learned from 15 years of free-air CO₂ enrichment (FACE)? A meta-analytic review of the responses of photosynthesis, canopy properties and plant production to rising CO₂. *N. Phytol.* **165**, 351–371 (2005).

4. Raven, J. A., Cockell, C. S. & De La Rocha, C. L. The evolution of inorganic carbon concentrating mechanisms in photosynthesis. *Phil. Trans. R. Soc. B* **363**, 2641–2650 (2008).
5. Freeman Rosenzweig, E. S. et al. The eukaryotic CO₂-concentrating organelle is liquid-like and exhibits dynamic reorganization. *Cell* **171**, 148–162 (2017).
6. Badger, M. R. et al. The diversity and coevolution of Rubisco, plastids, pyrenoids, and chloroplast-based CO₂-concentrating mechanisms in algae. *Can. J. Bot.* **76**, 1052–1071 (1998).
7. Villarreal, J. C. & Renner, S. S. Hornwort pyrenoids, carbon-concentrating structures, evolved and were lost at least five times during the last 100 million years. *Proc. Natl Acad. Sci. USA* **109**, 18873–18878 (2012).
8. Wang, Y., Stessman, D. J. & Spalding, M. H. The CO₂ concentrating mechanism and photosynthetic carbon assimilation in limiting CO₂: how *Chlamydomonas* works against the gradient. *Plant J. Cell Mol. Biol.* **82**, 429–448 (2015).
9. Raven, J. A. CO₂-concentrating mechanisms: a direct role for thylakoid lumen acidification? *Plant Cell Environ.* **20**, 147–154 (1997).
10. Mackinder, L. C. et al. A repeat protein links Rubisco to form the eukaryotic carbon-concentrating organelle. *Proc. Natl Acad. Sci. USA* **113**, 5958–5963 (2016).
11. Wunder, T., Cheng, S. L. H., Lai, S. K., Li, H. Y. & Mueller-Cajar, O. The phase separation underlying the pyrenoid-based microalgal Rubisco supercharger. *Nat. Commun.* **9**, 5076 (2018).
12. Atkinson, N. et al. The pyrenoid linker protein EPYC1 phase separates with hybrid *Arabidopsis*–*Chlamydomonas* Rubisco through interactions with the algal Rubisco small subunit. *J. Exp. Bot.* **70**, 5271–5285 (2019).
13. Taylor, T. C., Backlund, A., Bjorhall, K., Spreitzer, R. J. & Andersson, I. First crystal structure of Rubisco from a green alga, *Chlamydomonas reinhardtii*. *J. Biol. Chem.* **276**, 48159–48164 (2001).
14. Duff, A. P., Andrews, T. J. & Curmi, P. M. The transition between the open and closed states of Rubisco is triggered by the inter-phosphate distance of the bound bisphosphate. *J. Mol. Biol.* **298**, 903–916 (2000).
15. Meyer, M. T. et al. Rubisco small-subunit α -helices control pyrenoid formation in *Chlamydomonas*. *Proc. Natl Acad. Sci. USA* **109**, 19474–19479 (2012).
16. Engel, B. D. et al. Native architecture of the *Chlamydomonas* chloroplast revealed by in situ cryo-electron tomography. *eLife* **4**, e04889 (2015).
17. Goodenough, U. W. & Levine, R. P. Chloroplast structure and function in ac-20, a mutant strain of *Chlamydomonas reinhardtii*. 3. Chloroplast ribosomes and membrane organization. *J. Cell Biol.* **44**, 547–562 (1970).
18. Ma, Y., Pollock, S. V., Xiao, Y., Cunnusamy, K. & Moroney, J. V. Identification of a novel gene, CIA6, required for normal pyrenoid formation in *Chlamydomonas reinhardtii*. *Plant Physiol.* **156**, 884–896 (2011).
19. Caspari, O. D. et al. Pyrenoid loss in *Chlamydomonas reinhardtii* causes limitations in CO₂ supply, but not thylakoid operating efficiency. *J. Exp. Bot.* **68**, 3903–3913 (2017).
20. Li, P. et al. Phase transitions in the assembly of multivalent signalling proteins. *Nature* **483**, 336–340 (2012).
21. Borkhsenius, O. N., Mason, C. B. & Moroney, J. V. The intracellular localization of ribulose-1,5-bisphosphate carboxylase/oxygenase in *Chlamydomonas reinhardtii*. *Plant Physiol.* **116**, 1585–1591 (1998).
22. Turkina, M. V., Blanco-Rivero, A., Vainonen, J. P., Vener, A. V. & Villarejo, A. CO₂ limitation induces specific redox-dependent protein phosphorylation in *Chlamydomonas reinhardtii*. *Proteomics* **6**, 2693–2704 (2006).
23. Meyer, M. T. et al. Assembly of the algal CO₂-fixing organelle, the pyrenoid, is guided by a Rubisco-binding motif. *Sci. Adv.* <https://doi.org/10.1126/sciadv.abd2408> (in the press).
24. Cai, F. et al. Advances in understanding carboxysome assembly in *Prochlorococcus* and *Synechococcus* implicate CsoS2 as a critical component. *Life (Basel)* **5**, 1141–1171 (2015).
25. Oltrogge, L. M. et al. Multivalent interactions between CsoS2 and Rubisco mediate alpha-carboxysome formation. *Nat. Struct. Mol. Biol.* **27**, 281–287 (2020).
26. Long, B. M., Badger, M. R., Whitney, S. M. & Price, G. D. Analysis of carboxysomes from *Synechococcus* PCC7942 reveals multiple Rubisco complexes with carboxysomal proteins CcmM and CcaA. *J. Biol. Chem.* **282**, 29323–29335 (2007).
27. Wang, H. et al. Rubisco condensate formation by CcmM in beta-carboxysome biogenesis. *Nature* **566**, 131–135 (2019).
28. Hennacy, J. H. & Jonikas, M. C. Prospects for engineering biophysical CO₂ concentrating mechanisms into land plants to enhance yields. *Annu. Rev. Plant Biol.* <https://doi.org/10.1146/annurev-arplant-081519-040100> (2020).
29. Long, B. M. et al. Carboxysome encapsulation of the CO₂-fixing enzyme Rubisco in tobacco chloroplasts. *Nat. Commun.* **9**, 3570 (2018).
30. Lin, M. T., Occhialini, A., Andralojc, P. J., Parry, M. A. & Hanson, M. R. A faster Rubisco with potential to increase photosynthesis in crops. *Nature* **513**, 547–550 (2014).
31. Atkinson, N. et al. Introducing an algal carbon-concentrating mechanism into higher plants: location and incorporation of key components. *Plant Biotechnol. J.* **14**, 1302–1315 (2016).
32. Hanson, M. R., Gray, B. N. & Ahner, B. A. Chloroplast transformation for engineering of photosynthesis. *J. Exp. Bot.* **64**, 731–742 (2013).
33. Raven, J. A., Beardall, J. & Sanchez-Baracaldo, P. The possible evolution and future of CO₂-concentrating mechanisms. *J. Exp. Bot.* **68**, 3701–3716 (2017).
34. Kropat, J. et al. A revised mineral nutrient supplement increases biomass and growth rate in *Chlamydomonas reinhardtii*. *Plant J. Cell Mol. Biol.* **66**, 770–780 (2011).
35. Khrebtukova, I. & Spreitzer, R. J. Elimination of the *Chlamydomonas* gene family that encodes the small subunit of ribulose-1,5-bisphosphate carboxylase/oxygenase. *Proc. Natl Acad. Sci. USA* **93**, 13689–13693 (1996).
36. Zhang, R. et al. High-throughput genotyping of green algal mutants reveals random distribution of mutagenic insertion sites and endonucleolytic cleavage of transforming DNA. *Plant Cell* **26**, 1398–1409 (2014).
37. BIAevaluation 4.1.1 (Biacore AB, 2020).
38. Zheng, S. Q. et al. MotionCor2: anisotropic correction of beam-induced motion for improved cryo-electron microscopy. *Nat. Methods* **14**, 331–332 (2017).
39. Rohou, A. & Grigorieff, N. CTFIND4: fast and accurate defocus estimation from electron micrographs. *J. Struct. Biol.* **192**, 216–221 (2015).
40. Zivanov, J. et al. New tools for automated high-resolution cryo-EM structure determination in RELION-3. *eLife* **7**, e42166 (2018).
41. Grant, T., Rohou, A. & Grigorieff, N. cisTEM, user-friendly software for single-particle image processing. *eLife* **7**, e35383 (2018).
42. Punjani, A., Rubinstein, J. L., Fleet, D. J. & Brubaker, M. cryoSPARC: algorithms for rapid unsupervised cryo-EM structure determination. *Nat. Methods* **14**, 290–296 (2017).
43. Punjani, A., Brubaker, M. A. & Fleet, D. J. Building proteins in a day: efficient 3D molecular structure estimation with electron cryomicroscopy. *IEEE Trans. Pattern Anal. Mach. Intell.* **39**, 706–718 (2017).
44. Pettersen, E. F. et al. UCSF Chimera—a visualization system for exploratory research and analysis. *J. Comput. Chem.* **25**, 1605–1612 (2004).
45. Emsley, P., Lohkamp, B., Scott, W. G. & Cowtan, K. Features and development of COOT. *Acta Crystallogr. D* **66**, 486–501 (2010).
46. Drozdetskiy, A., Cole, C., Procter, J. & Barton, G. J. JPred4: a protein secondary structure prediction server. *Nucleic Acids Res.* **43**, W389–W394 (2015).
47. Adams, P. D. et al. PHENIX: a comprehensive Python-based system for macromolecular structure solution. *Acta Crystallogr. D* **66**, 213–221 (2010).
48. Chen, V. B. et al. MolProbity: all-atom structure validation for macromolecular crystallography. *Acta Crystallogr. D* **66**, 12–21 (2010).
49. Sueoka, N. Mitotic replication of deoxyribonucleic acid in *Chlamydomonas reinhardtii*. *Proc. Natl Acad. Sci. USA* **46**, 83–91 (1960).
50. Catanzariti, A. M., Soboleva, T. A., Jans, D. A., Board, P. G. & Baker, R. T. An efficient system for high-level expression and easy purification of authentic recombinant proteins. *Protein Sci.* **13**, 1331–1339 (2004).
51. Ewalt, K. L., Hendrick, J. P., Houry, W. A. & Hartl, F. U. In vivo observation of polypeptide flux through the bacterial chaperonin system. *Cell* **90**, 491–500 (1997).
52. Baker, R. T. et al. in *Ubiquitin and Protein Degradation, Part A: Methods in Enzymology* (eds Deshaies, R. J.) 540–554 (Academic Press, 2005).
53. Genkov, T., Meyer, M., Griffiths, H. & Spreitzer, R. J. Functional hybrid Rubisco enzymes with plant small subunits and algal large subunits: engineered rbcS cDNA for expression in *Chlamydomonas*. *J. Biol. Chem.* **285**, 19833–19841 (2010).
54. Gibson, D. G. et al. Enzymatic assembly of DNA molecules up to several hundred kilobases. *Nat. Methods* **6**, 343–345 (2009).
55. Li, X. et al. A genome-wide algal mutant library and functional screen identifies genes required for eukaryotic photosynthesis. *Nat. Genet.* **51**, 627–635 (2019).
56. Martinez-Sanchez, A. et al. Template-free detection and classification of membrane-bound complexes in cryo-electron tomograms. *Nat. Methods* <https://doi.org/10.1038/s41592-019-0675-5> (2020).
57. Cheng, S., Cetinkaya, M. & Grater, F. How sequence determines elasticity of disordered proteins. *Biophys. J.* **99**, 3863–3869 (2010).

Acknowledgements

We thank J. Wu, N. Yan, L. Mackinder, C. Brangwynne and members of the Jonikas laboratory for helpful discussions; N. Wingreen, S. Ramundo, J. Hennacy, E. Franklin and A. Wilson for constructive feedback on the manuscript; W. Baumeister and J. Plitzko for providing support and cryo-electron tomography instrumentation; and M. Schaffer for help with acquiring the cryo-electron tomography data, previously published in ref. 5. This project was funded by National Science Foundation (nos IOS-1359682 and MCB-1935444), National Institutes of Health (no. DP2-GM-119137), and Simons Foundation and Howard Hughes Medical Institute (no. 55108535) grants to M.C.J.; a Deutsche Forschungsgemeinschaft grant (EN 1194/1-1 as part of FOR2092) to B.D.E.; a Ministry of Education (MOE Singapore) Tier 2 grant (no. MOE2018-T2-2-059)

to O.M.-C.; UK Biotechnology and Biological Sciences Research Council (no. BB/S015531/1) and Leverhulme Trust (no. RPG-2017-402) grants to A.J.M. and N.A.; NIH grant no. R01GM071574 to F.M.H.; a Deutsche Forschungsgemeinschaft fellowship (no. PO2195/1-1) to S.A.P.; and a National Institute of General Medical Sciences of the National Institutes of Health (no. T32GM007276) training grant to V.K.C. The content is solely the responsibility of the authors and does not necessarily represent the official view of the National Institutes of Health.

Author contributions

S.H., P.D.J., V.K.C., F.M.H., T.W., O.M.-C., B.D.E. and M.C.J. designed the experiments. S.H. identified EPYC1's Rubisco-binding regions by peptide tiling array and surface plasmon resonance. S.H. and S.A.P. prepared the Rubisco and EPYC1 peptide samples for single-particle cryo-electron microscopy. S.H., S.A.P. and G.H. prepared the Rubisco samples for peptide tiling array and surface plasmon resonance experiments. H.-T.C., D.M. and Z.Y. performed the cryo-electron microscopy grid preparation, sample screening, data acquisition, image processing, reconstruction and map generation. D.M. and P.D.J. carried out the single-particle model building and fitting and refinement. S.H., H.-T.C., D.M., P.D.J., F.M.H. and M.C.J. analysed the structures. S.H. and W.P. analysed EPYC1 binding to Rubisco by peptide substitution array and surface plasmon resonance experiments. T.W. performed the in vitro reconstitution phase separation experiments. N.A. and A.J.M. performed the yeast two-hybrid experiments. S.H. and M.T.M. made the Rubisco small subunit point mutants. S.H. performed the spot test experiments. M.T.M.

performed the transmission electron microscopy. A.M.-S. performed the cryo-electron tomography data analysis and modelling. S.H. and M.C.J. wrote the manuscript. All authors read and commented on the manuscript.

Competing interests

Princeton University and HHMI have submitted a provisional patent application on aspects of the findings.

Additional information

Extended data is available for this paper at <https://doi.org/10.1038/s41477-020-00811-y>.

Supplementary information is available for this paper at <https://doi.org/10.1038/s41477-020-00811-y>.

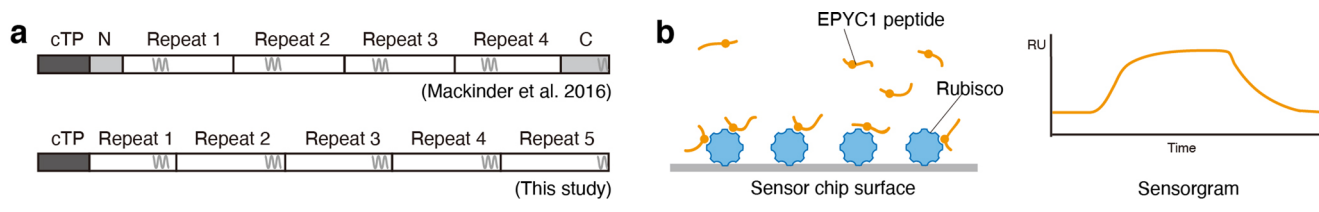
Correspondence and requests for materials should be addressed to M.C.J.

Peer review information *Nature Plants* thanks Jean-David Rochaix and the other, anonymous, reviewer(s) for their contribution to the peer review of this work.

Reprints and permissions information is available at www.nature.com/reprints.

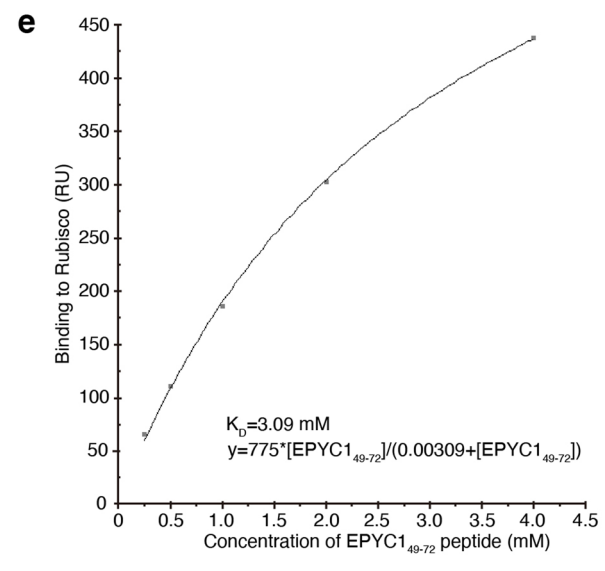
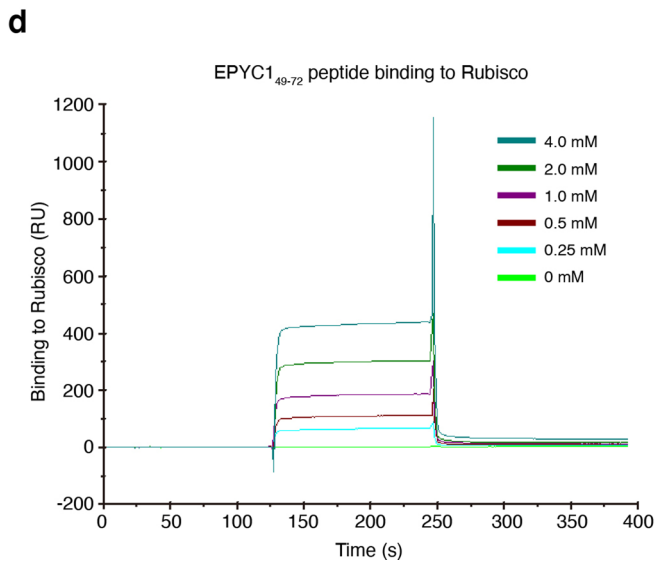
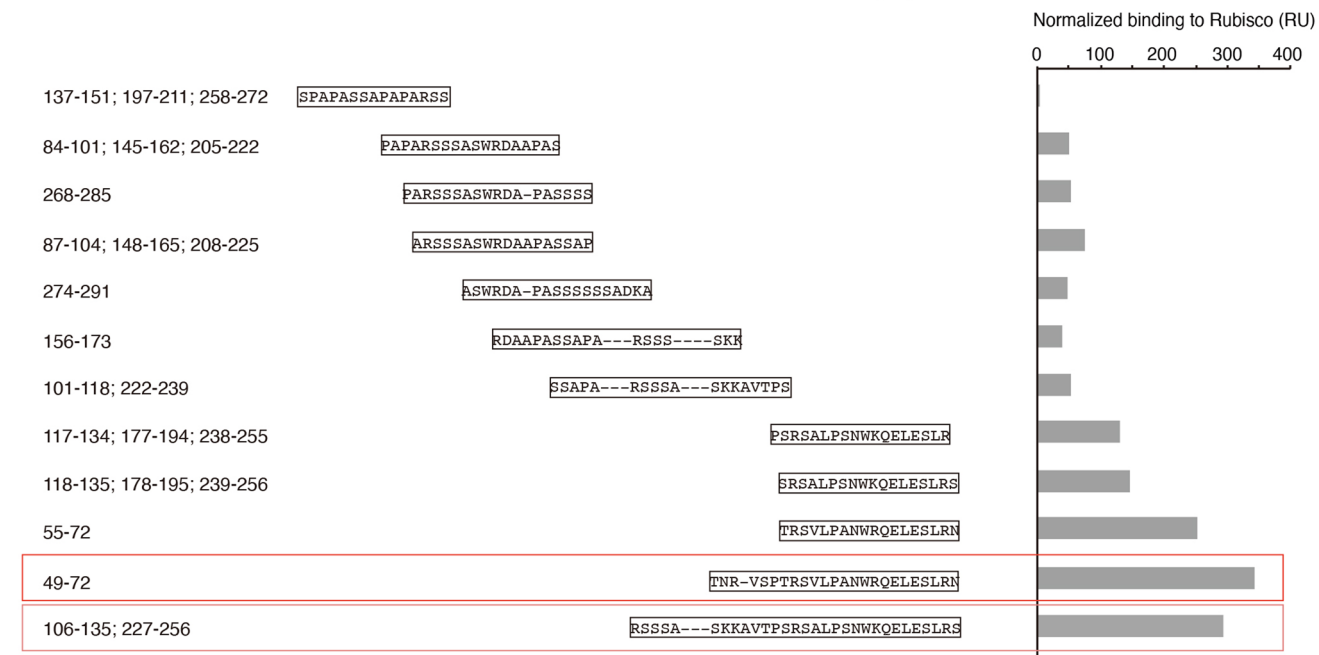
Publisher's note Springer Nature remains neutral with regard to jurisdictional claims in published maps and institutional affiliations.

© The Author(s), under exclusive licence to Springer Nature Limited 2020



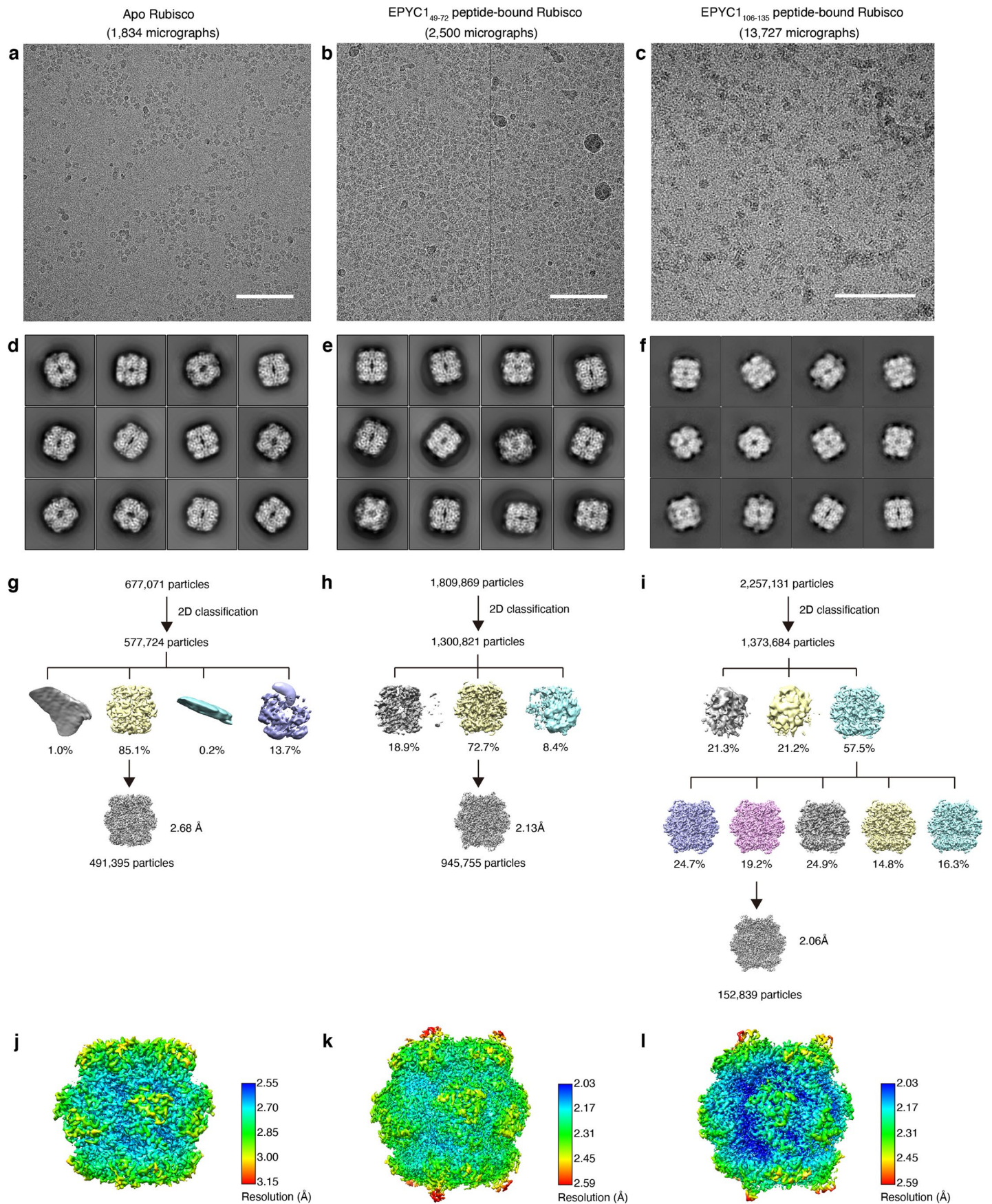
c

1	MATISSMRVGAASRVVVSGRVKTVKVA	27	cTP
28	ARGSWRESSTATVQAS---RASSA---TNR-VSPTRSVLPANWRQELSLRNGNGS	76	Unit 1
77	SSAASSAPAPARSSSASWRDAAPASSAPA---RSSSA---SKKAVTPSRALPSNWKQELSLRS--SS	137	Unit 2
138	PAPASSAPAPARSSSASWRDAAPASSAPA---RSSS---SKKAVTPSRALPSNWKQELSLRS--SS	197	Unit 3
198	PAPASSAPAPARSSSASWRDAAPASSAPA---RSSSA---SKKAVTPSRALPSNWKQELSLRS-N-S	258	Unit 4
259	PAPASSAPAPARSSSASWRDA-PASSSSSSADKAGTNPWTGKSKPEIKRTALPADWRKGL*	317	Unit 5



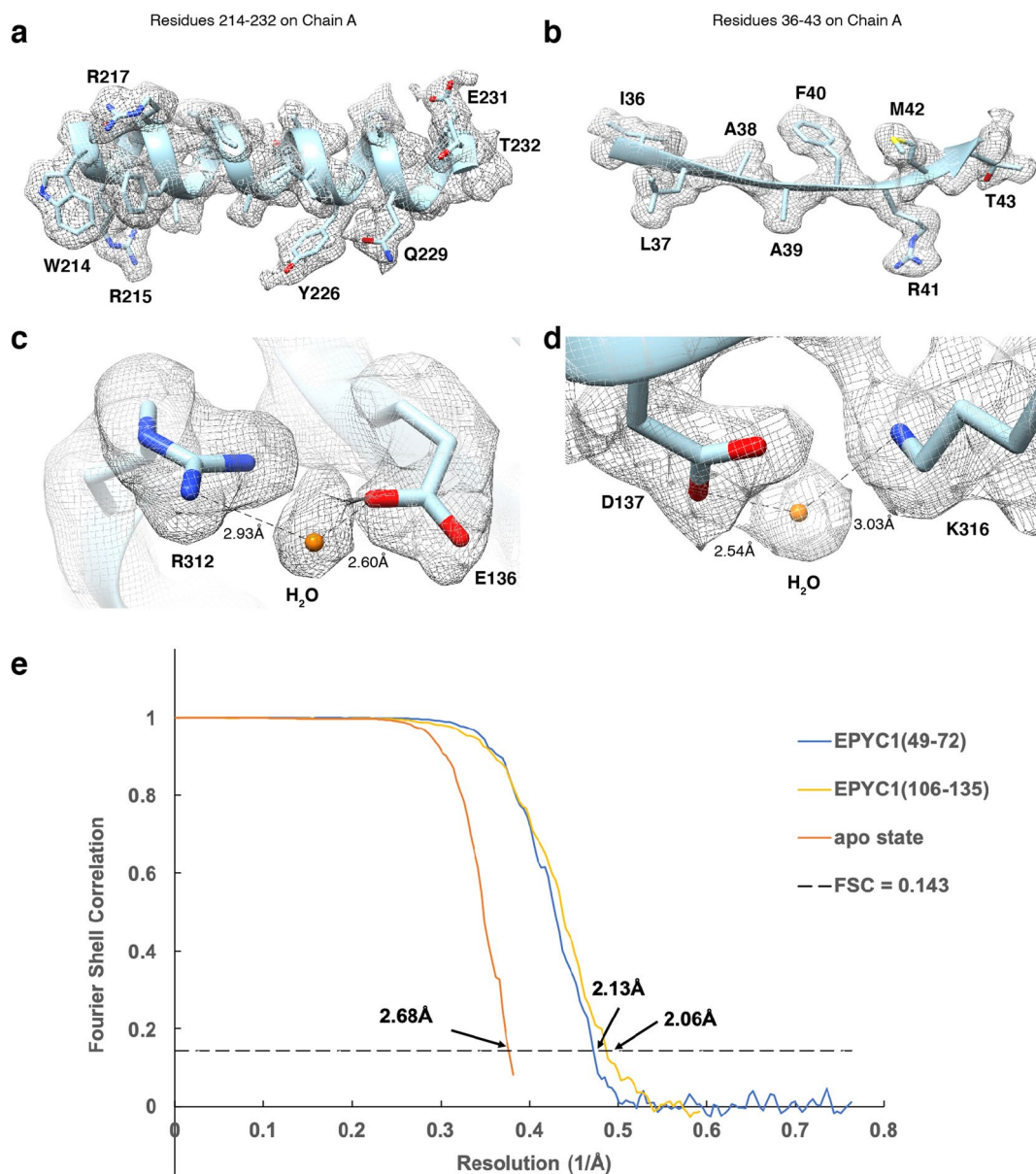
Extended Data Fig. 1 | See next page for caption.

Extended Data Fig. 1 | The EPYC1 peptides with the highest binding affinities to Rubisco were chosen for structural studies. **a**, Diagram indicating the differences between the previously defined sequence repeats¹⁰ and the newly defined sequence repeats on full-length EPYC1. **b**, To verify the Rubisco-binding regions on EPYC1, surface plasmon resonance (SPR) was used to measure the binding of EPYC1 peptides to Rubisco. Purified Rubisco was immobilized on a sensor surface, and the EPYC1 peptides in solution were injected over the surface. The binding activity was recorded in real time in a sensorgram. **c**, The peptides used in SPR experiments are shown aligned to the sequence as shown in Fig. 1. The Rubisco-binding signal from the SPR experiment of each peptide is shown after normalization to the peptide's molecular weight. EPYC1₄₉₋₇₂ (boxed in red) and EPYC1₁₀₆₋₁₃₅ (boxed in pink) were chosen for structural studies based on their reproducible high Rubisco binding signal. **d**, The Rubisco-binding response of the EPYC1₄₉₋₇₂ peptide at different concentrations was measured by SPR. **e**, The binding responses shown in (d) were fitted to estimate the K_D of EPYC1₄₉₋₇₂ peptide binding to Rubisco.

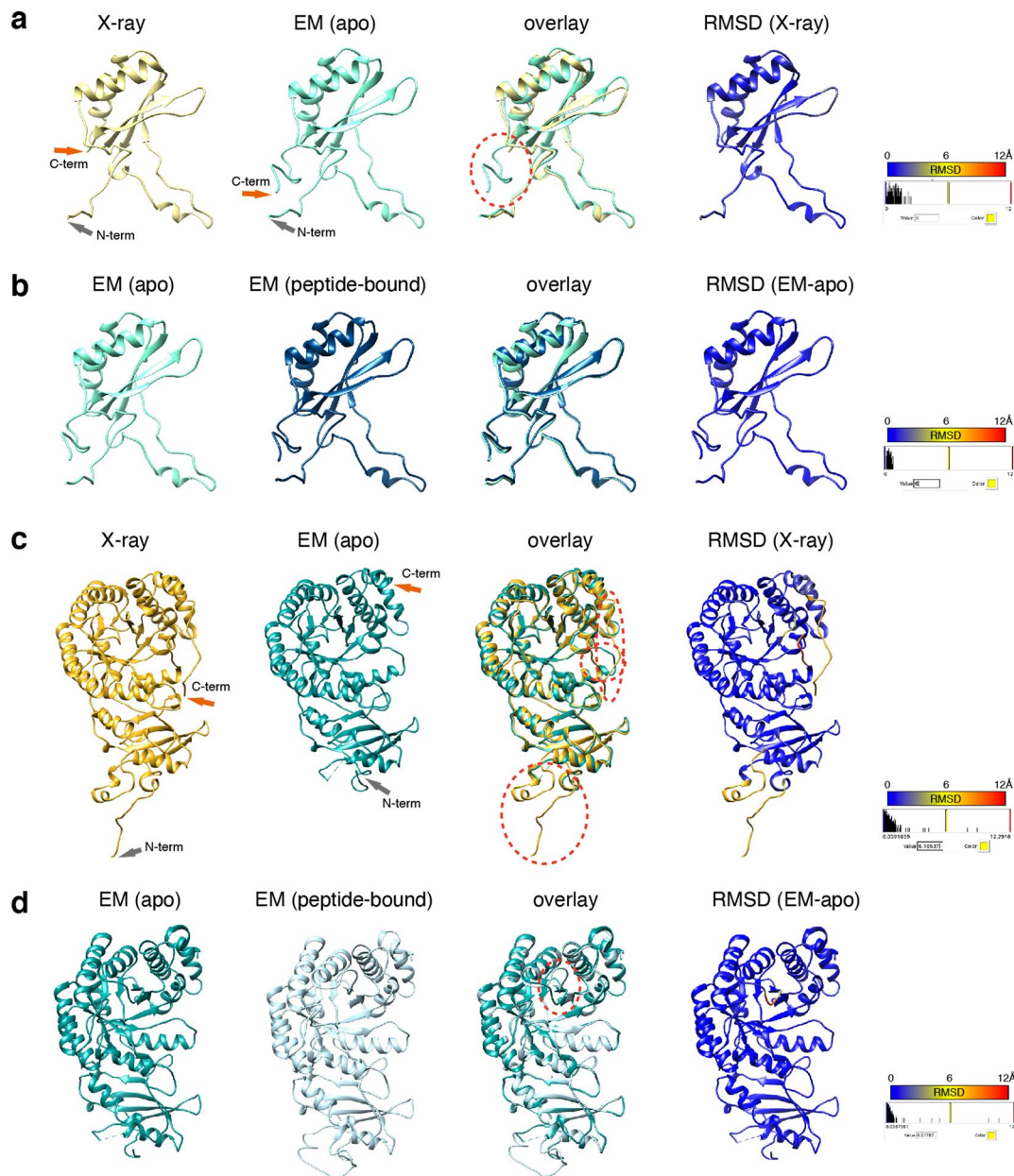


Extended Data Fig. 2 | See next page for caption.

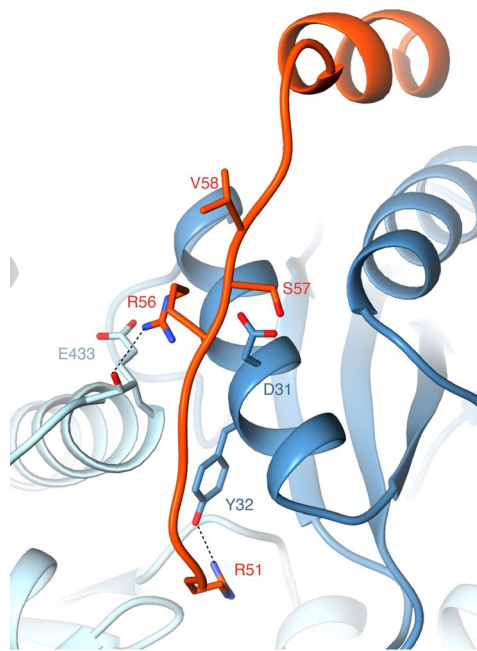
Extended Data Fig. 2 | Single-particle cryo-EM data collection and image processing procedure. **a-c**, Representative micrographs of the apo Rubisco sample (a), the Rubisco-EPYC1₄₉₋₇₂ complex (b) and the Rubisco-EPYC1₁₀₆₋₁₃₅ complex (c). Scale bars = 100 nm. **d-f**, Representative 2D class averages of the apo Rubisco sample (d), the Rubisco-EPYC1₄₉₋₇₂ complexes (e) and the Rubisco-EPYC1₁₀₆₋₁₃₅ complexes (f). **g-i**, Overview of the workflow for single-particle data processing for the apo Rubisco sample (g), the Rubisco-EPYC1₄₉₋₇₂ sample (h) and the Rubisco-EPYC1₁₀₆₋₁₃₅ sample (i). **j-l**, Local resolution estimation of the final refined apo Rubisco map (j), the final refined Rubisco-EPYC1₄₉₋₇₂ complex map (k) and the final refined Rubisco-EPYC1₁₀₆₋₁₃₅ complex map (l).



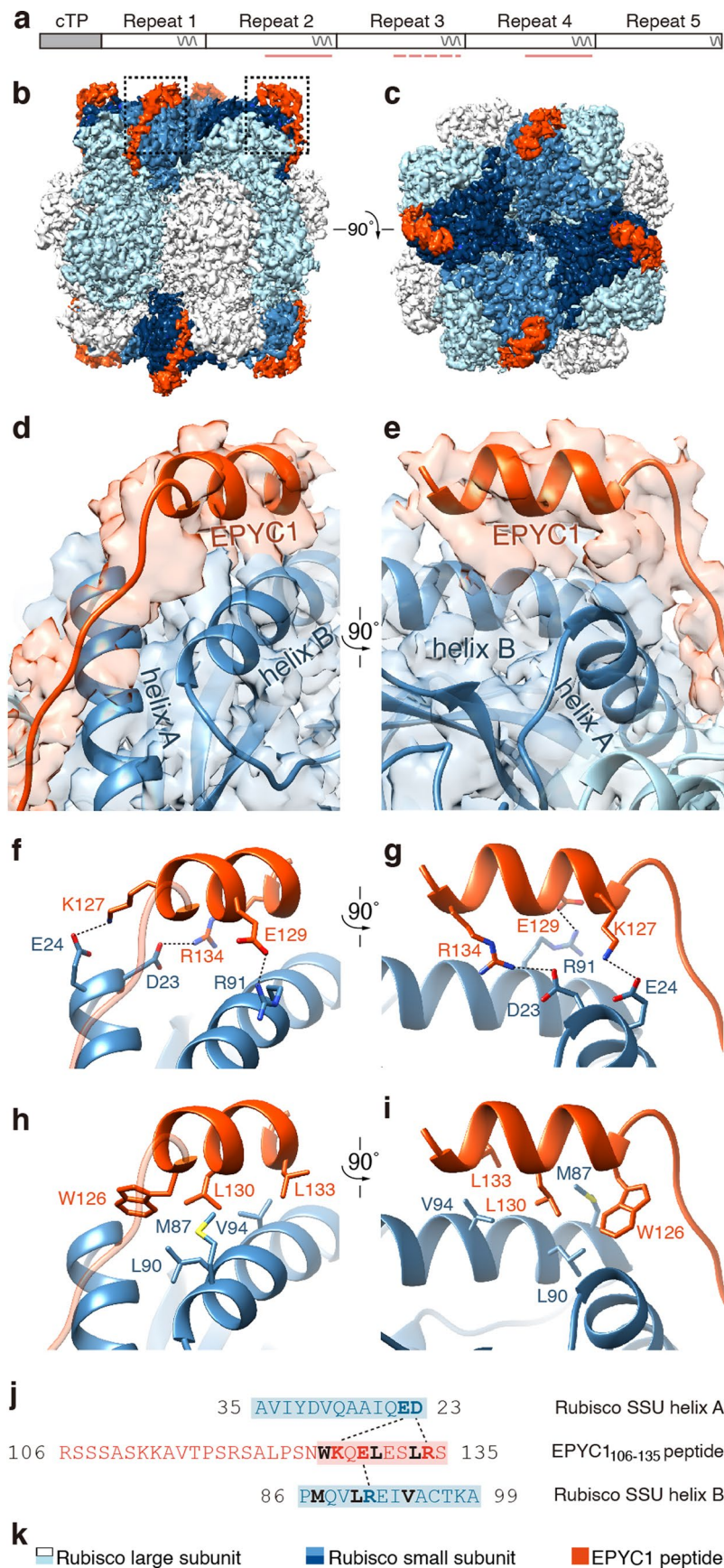
Extended Data Fig. 3 | Cryo-EM analysis and resolution of apo Rubisco and Rubisco-EPYC1 peptide complexes in this study. a-b, Representative cryo-EM density quality showing an α -helix of residues 214-232 in chain A (one of the Rubisco large subunits) (a) and a β -sheet of residues 36-43 in chain A (b) of the Rubisco-EPYC1₄₉₋₇₂ density map and structural model. The densities are shown as meshwork in gray. The backbones of the structural model are in ribbon representation, and side chains are shown in stick representation. **c-d**, Representative cryo-EM density quality showing water molecules as orange spheres. One water molecule between R312 and E136 on chain A is shown in panel c, and another water molecule between D137 and K316 on chain A is shown in panel d. **e**, Fourier shell correlation (FSC) curves of the final density maps of apo Rubisco and the Rubisco-EPYC1 peptide complexes.



Extended Data Fig. 4 | Comparison of our EM structure of apo Rubisco and the published X-ray crystallography structure (1gk8) of Rubisco purified from *Chlamydomonas reinhardtii*¹³, and comparison of our EM structure of apo Rubisco and Rubisco bound with EPYC1₄₉₋₇₂ peptide. **a, Comparison of the structure of the small subunit of apo Rubisco obtained here by EM with 1gk8. The EM structure has additional C-terminus density past residue 126, circled by a red dashed line. **b**, Comparison of our two EM structures of the small subunit: from apo Rubisco and from EPYC1₄₉₋₇₂ peptide-bound Rubisco. **c**, Comparison of the structure of the large subunit of apo Rubisco obtained here by EM with 1gk8. The three major differences found between the X-ray structure and the EM structure of the large subunit are circled with red dashed lines. **d**, Comparison of our two EM structures of the large subunit: from apo Rubisco and from EPYC1₄₉₋₇₂ peptide-bound Rubisco. The major difference found between the EPYC1₄₉₋₇₂ peptide-bound structure and the apo EM structure was the loop between K175 and L180 of the large subunit, which is shown circled by a red dashed line.**

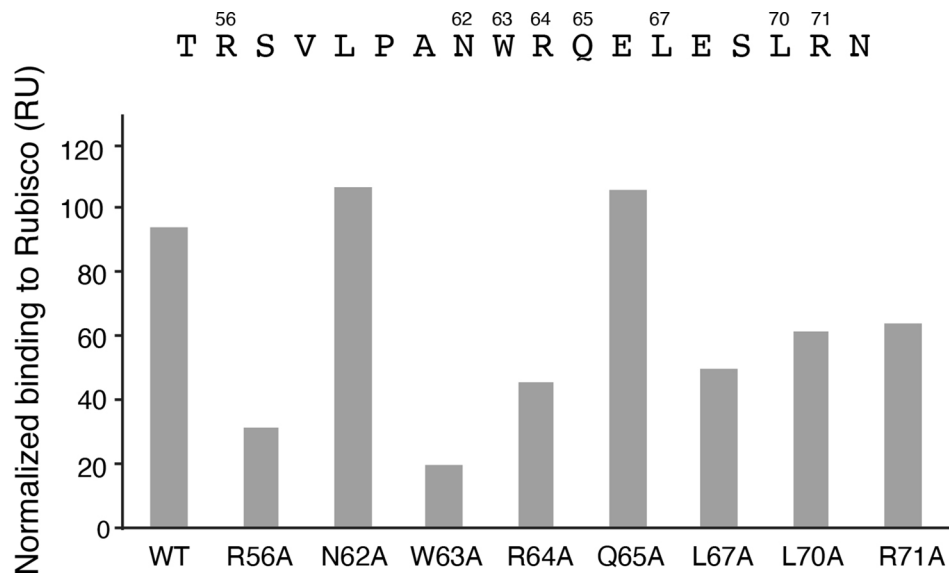


Extended Data Fig. 5 | Additional residues may contribute to the interaction between EPYC1 and Rubisco. Our Rubisco-EPYC1₄₉₋₇₂ peptide structure suggests that R56 of the EPYC1₄₉₋₇₂ peptide may interact with D31 of the Rubisco small subunit and E433 of the Rubisco large subunit (the atoms of the backbone of E433 are also shown to display the possible interaction). R51 of the EPYC1₄₉₋₇₂ peptide may form a salt bridge with Y32 of the Rubisco small subunit. Residues S57 and V58 of the EPYC1₄₉₋₇₂ peptide are close to D31 in the structure, which may explain why replacing either of these residues with a negatively charged residue disrupts binding (Fig. 4a).

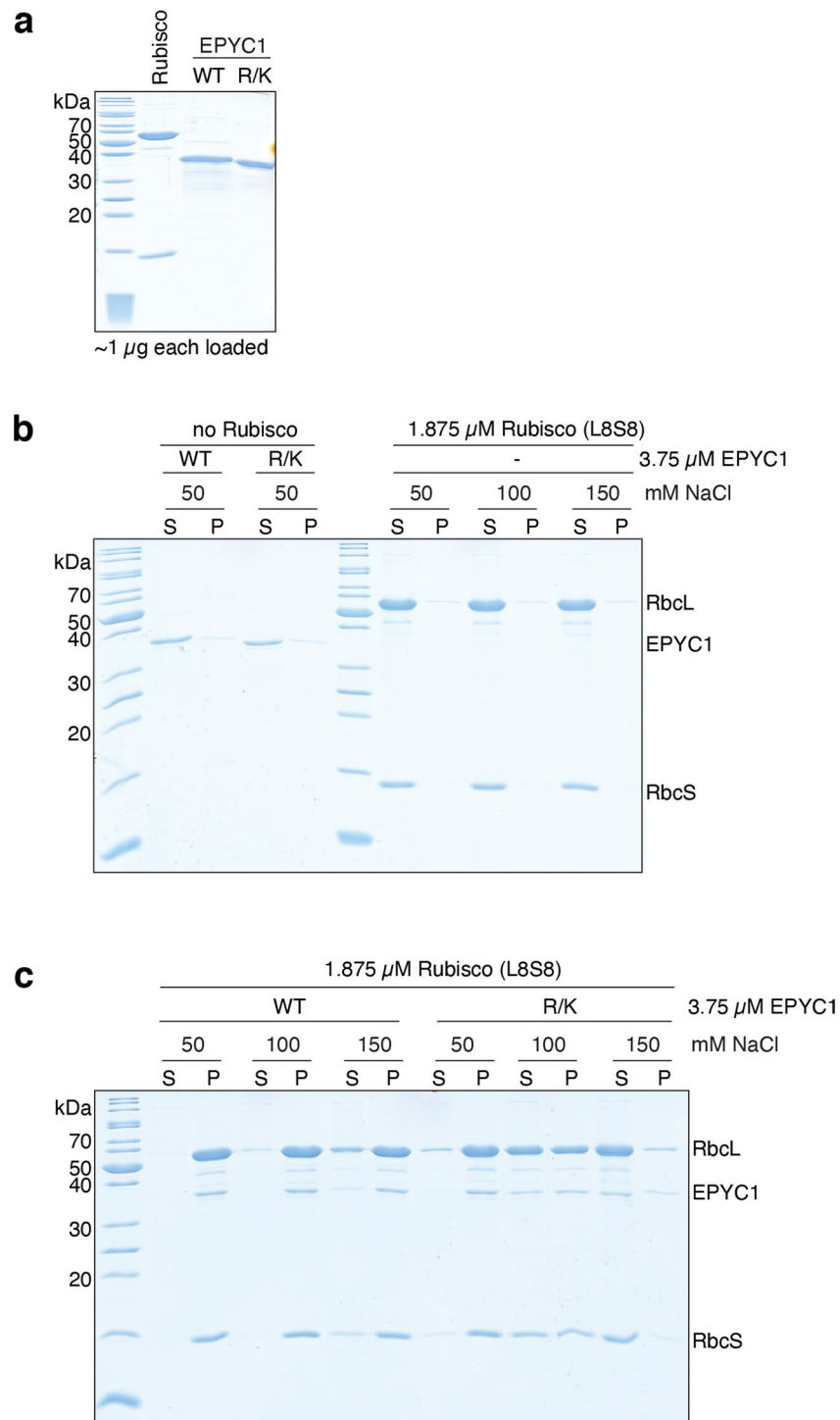


Extended Data Fig. 6 | See next page for caption.

Extended Data Fig. 6 | The EPYC1₁₀₆₋₁₃₅ peptide binds to Rubisco small subunit α -helices via salt bridges and a hydrophobic pocket in a similar manner to the EPYC1₄₉₋₇₂ peptide. **a**, The EPYC1₁₀₆₋₁₃₅ peptide represents the second, third and fourth Rubisco-binding regions of EPYC1 indicated by pink lines and dash line (the peptide is a perfect match to the second and fourth Rubisco-binding regions, and there is a one-amino acid difference between the peptide and the third repeat). **b-c**, Side view (**b**) and top view (**c**) of the density map of the EPYC1₁₀₆₋₁₃₅ peptide-Rubisco complex. Dashes in panel **b** indicate regions shown in panels **d-i**. **d-e**, Front (**d**) and side (**e**) views of the EPYC1₁₀₆₋₁₃₅ peptide (red) bound to the two α -helices of the Rubisco small subunit (blue). **f-g**, Three pairs of residues form salt bridges between the helix of the EPYC1₁₀₆₋₁₃₅ peptide and the helices on the Rubisco small subunit. Shown are front (**f**) and side (**g**) views as in panel **d** and panel **e**. The distances from EPYC1 K127, R134 and E129 to Rubisco small subunit E24, D23 and R91 are 2.96 Å, 3.17 Å, and 2.68 Å, respectively. **h-i**, A hydrophobic pocket is formed by three residues of the EPYC1₁₀₆₋₁₃₅ peptide and three residues of helix B of the Rubisco small subunit. Shown are front (**h**) and side (**i**) views as in panel **d** and panel **e**. **j**, Summary of the interactions observed between the EPYC1₁₀₆₋₁₃₅ peptide and the two α -helices of the Rubisco small subunit. Helices are highlighted; the residues mediating interactions are bold; salt bridges are shown as dotted lines; residues contributing to the hydrophobic pocket are shown in black. **k**, Color keys used in this figure.

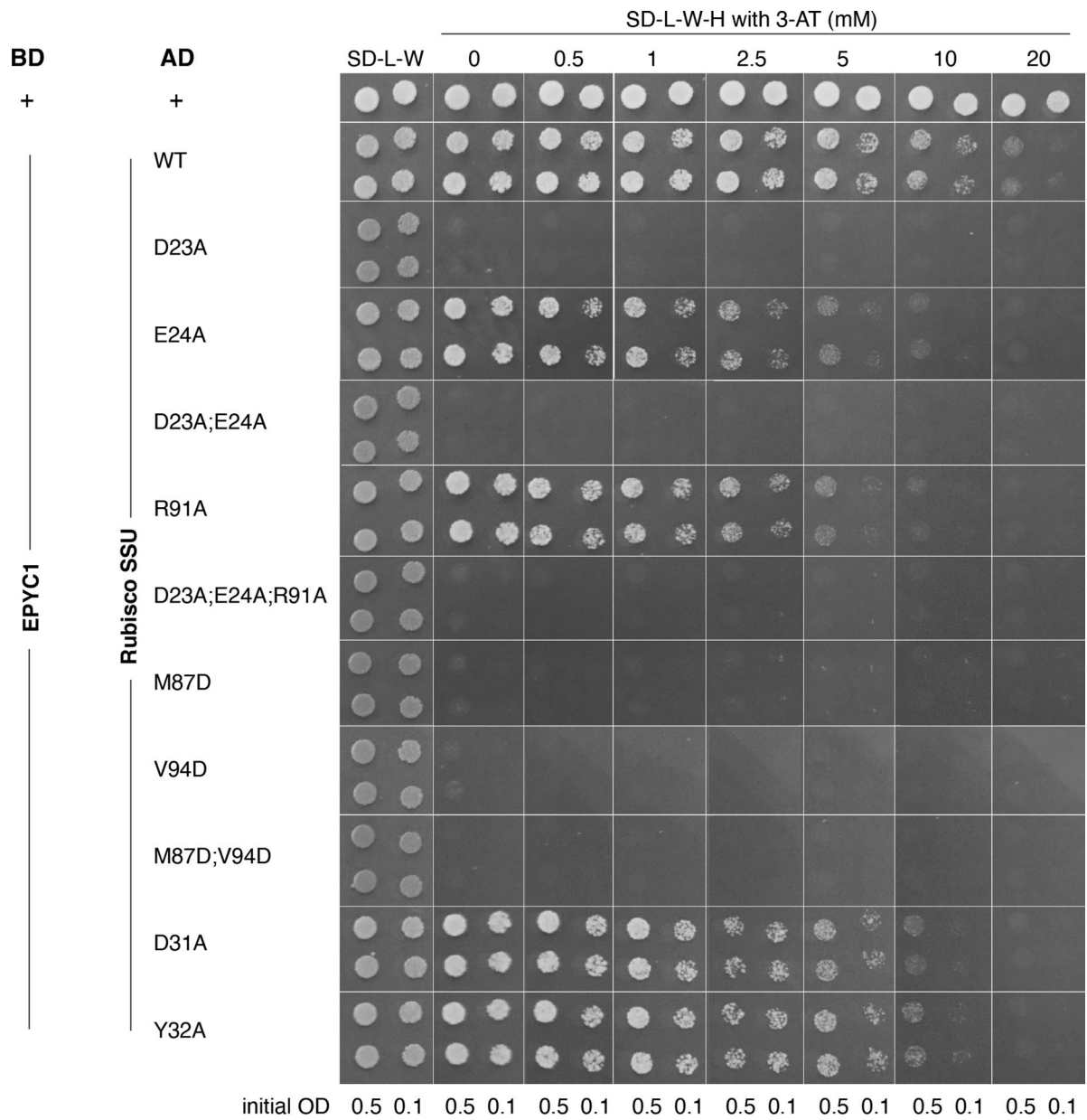


Extended Data Fig. 7 | Surface plasmon resonance analysis of binding of point mutants of EPYC1₅₅₋₇₂ to Rubisco. The wild-type (WT) peptide or peptides with the indicated mutations were synthesized, and their Rubisco-binding signal was measured by surface plasmon resonance.

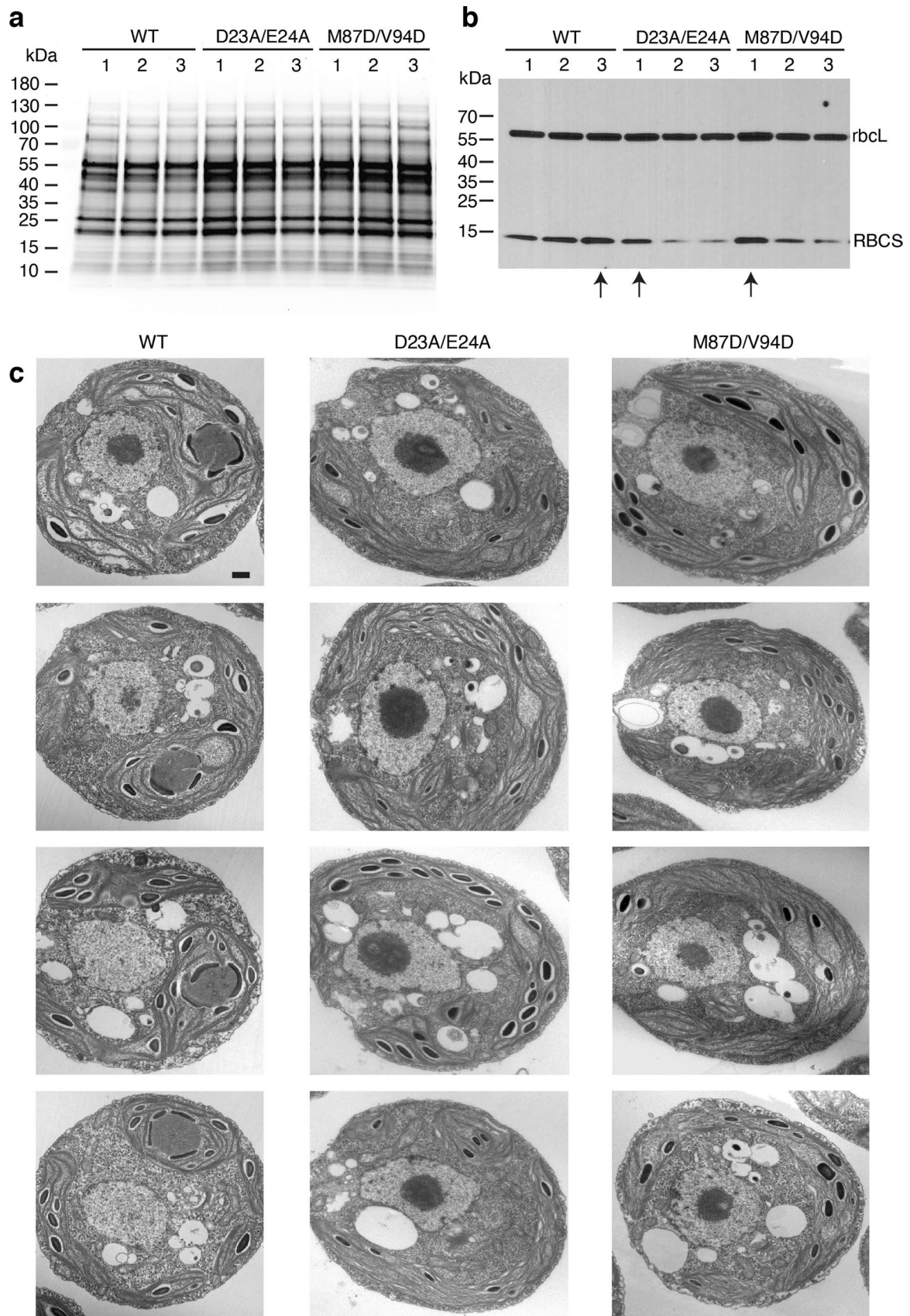


Extended Data Fig. 8 | Interface residues on EPYC1 identified by cryo-EM are important for binding and phase separation of EPYC1 and Rubisco.

a, SDS-PAGE analysis of purified proteins used for *in vitro* phase separation experiments. WT = wild-type EPYC1; R/K = EPYC1^{R64A/K127A/K187A/K248A/R314}. **b-c**, A droplet sedimentation assay was used as a readout of phase separation complementary to the microscopy analyses shown in Fig. 4b. Proteins at indicated concentrations were mixed and incubated for 10 minutes, then condensates were pelleted by centrifugation. Supernatant (S) and pellet (P) fractions were run on a denaturing gel. The negative controls with no Rubisco or with no EPYC1 are shown in (b), and the wild-type Rubisco with wild-type EPYC1 or mutant EPYC1 are shown in (c). Data shown here are representative of two independent replicates.



Extended Data Fig. 9 | Yeast two-hybrid assays of interactions between EPYC1 and wild-type or mutated Rubisco small subunit. Colonies are shown after 3 days growth on plates. A subset of the data shown in this figure is shown in Fig. 5a.



Extended Data Fig. 10 | See next page for caption.

Extended Data Fig. 10 | Selection of the Rubisco small subunit mutant strains for phenotype analysis. **a**, The Rubisco small subunit-less mutant T60 ($\Delta rbcS$) was transformed with DNA encoding wild-type and mutant Rubisco small subunits (RBCS) to produce candidate transformants with the genotypes $\Delta rbcS;RBCS^{WT}$, $\Delta rbcS;RBCS^{D23A/E24A}$, and $\Delta rbcS;RBCS^{M87D/V94D}$. Total protein extracts for three strains from each transformation were separated on a polyacrylamide gel. **b**, The gel shown in panel a was probed by Western blot using a polyclonal antibody mixture that detects both large and small Rubisco subunits. The experiments shown in panel a and b were performed once for selecting the candidate transformants with the highest RBCS expression level from each genotype, in case any phenotype may be caused by low expression level of Rubisco. Selected strains are indicated by an arrow below the lanes and were used for the subsequent phenotypic analyses shown in Fig. 5 and panel c. **c**, Additional representative TEM images of whole cells of the strains expressing wild-type, D23A/E24A, and M87D/V94D Rubisco small subunit. Scale bar = 500 nm. For each strain, at least 25 images (one image for one cell) were taken and showing similar results.

Reporting Summary

Nature Research wishes to improve the reproducibility of the work that we publish. This form provides structure for consistency and transparency in reporting. For further information on Nature Research policies, see our [Editorial Policies](#) and the [Editorial Policy Checklist](#).

Statistics

For all statistical analyses, confirm that the following items are present in the figure legend, table legend, main text, or Methods section.

n/a Confirmed

- The exact sample size (n) for each experimental group/condition, given as a discrete number and unit of measurement
- A statement on whether measurements were taken from distinct samples or whether the same sample was measured repeatedly
- The statistical test(s) used AND whether they are one- or two-sided
Only common tests should be described solely by name; describe more complex techniques in the Methods section.
- A description of all covariates tested
- A description of any assumptions or corrections, such as tests of normality and adjustment for multiple comparisons
- A full description of the statistical parameters including central tendency (e.g. means) or other basic estimates (e.g. regression coefficient) AND variation (e.g. standard deviation) or associated estimates of uncertainty (e.g. confidence intervals)
- For null hypothesis testing, the test statistic (e.g. F , t , r) with confidence intervals, effect sizes, degrees of freedom and P value noted
Give P values as exact values whenever suitable.
- For Bayesian analysis, information on the choice of priors and Markov chain Monte Carlo settings
- For hierarchical and complex designs, identification of the appropriate level for tests and full reporting of outcomes
- Estimates of effect sizes (e.g. Cohen's d , Pearson's r), indicating how they were calculated

Our web collection on [statistics for biologists](#) contains articles on many of the points above.

Software and code

Policy information about [availability of computer code](#)

Data collection

The following publicly available software was used
for single-particle cryo-electron microscopy: SerialEM 3.8.0 beta;
for peptide arrays: ImageQuant LAS-4000 control software 1.2; Typhoon FLA 9500 control software 1.0
for SPR: BIACORE 3000 control software 4.1

Data analysis

The following publicly available software was used
for single-particle cryo-electron microscopy: MotionCor2 1.3.0, CTFFIND 4.1.13, Relion 2.1 & 3.1-beta, cisTEM 1.0.0-beta, cryoSPARC 2.14.2, UCSF Chimera 1.12, COOT 0.8.9, JPred4, Phenix 1.13, MolProbity 4.5.1 and PyMOL 2.1.1;
for peptide arrays: ImageQuant TL 8.1;
for generating Chlamydomonas mutants of Rubisco small subunits: SnapGene 5.1.5;
for pyrenoid tomograms: PySeg 1.0;
for SPR: BIAevaluation 4.1.1

For manuscripts utilizing custom algorithms or software that are central to the research but not yet described in published literature, software must be made available to editors and reviewers. We strongly encourage code deposition in a community repository (e.g. GitHub). See the Nature Research [guidelines for submitting code & software](#) for further information.

Data

Policy information about [availability of data](#)

All manuscripts must include a [data availability statement](#). This statement should provide the following information, where applicable:

- Accession codes, unique identifiers, or web links for publicly available datasets
- A list of figures that have associated raw data
- A description of any restrictions on data availability

Fig.1, Fig.2, Fig.3, Fig.4 and Fig.6 have associated raw data.

Data availability:

For structural data:

EMDB-22401, PDB 7JN4, EMPIAR-10503;

EMDB-22308, PDB 7JFO, EMPIAR-10502;

EMDB-22462, PDB 7JSX, EMPIAR-10501;

EMD-3694.

For Chlamydomonas Rubisco small subunit point mutants and related plasmids:

CC-5616, CC-5617 and CC-5618; pSH001 and pSH002 (Chlamydomonas Resource Center)

Field-specific reporting

Please select the one below that is the best fit for your research. If you are not sure, read the appropriate sections before making your selection.

- Life sciences Behavioural & social sciences Ecological, evolutionary & environmental sciences

For a reference copy of the document with all sections, see [nature.com/documents/nr-reporting-summary-flat.pdf](https://www.nature.com/documents/nr-reporting-summary-flat.pdf)

Life sciences study design

All studies must disclose on these points even when the disclosure is negative.

Sample size	For cryo-EM structure determination we sought to take as many micrographs as we could given instrument time constraints. For each strain in the TEM experiments, we took more than 25 images of longitudinal sections across different cells. This sample size was guided by previous experience of the number of images needed to reliably see differences between cells.
Data exclusions	No data were excluded from the analysis.
Replication	For both peptide arrays, each peptide was represented by at least two spots on the same array, and these replicates were averaged during data analysis. Each array was incubated and analyzed at least twice, and all attempts at replication were successful. Each surface plasmon resonance (SPR) experiments was repeated at least twice and all attempts at replication were successful. The liquid-liquid phase separation assay was performed twice and each replicate showed similar results. The yeast two-hybrid assay was performed twice and each replicate showed similar results. The spot tests were performed three times and each replicate showed similar results. Transmission electron microscopy for each strain was performed on multiple cells from one culture for each strain and results were consistent across cells. For each strain, we took more than 25 images of different randomly-picked longitudinal sections across different cells.
Randomization	The locations of peptides on each peptide array were randomized. Samples for other experiments were not randomized.
Blinding	Peptide array spot positions were randomized and quantified by a second person who did not know the identities of the spots. For the other experiments, investigators were not blinded.

Reporting for specific materials, systems and methods

We require information from authors about some types of materials, experimental systems and methods used in many studies. Here, indicate whether each material, system or method listed is relevant to your study. If you are not sure if a list item applies to your research, read the appropriate section before selecting a response.

Materials & experimental systems

n/a	Involved in the study
<input type="checkbox"/>	<input checked="" type="checkbox"/> Antibodies
<input checked="" type="checkbox"/>	<input type="checkbox"/> Eukaryotic cell lines
<input checked="" type="checkbox"/>	<input type="checkbox"/> Palaeontology and archaeology
<input checked="" type="checkbox"/>	<input type="checkbox"/> Animals and other organisms
<input checked="" type="checkbox"/>	<input type="checkbox"/> Human research participants
<input checked="" type="checkbox"/>	<input type="checkbox"/> Clinical data
<input checked="" type="checkbox"/>	<input type="checkbox"/> Dual use research of concern

Methods

n/a	Involved in the study
<input checked="" type="checkbox"/>	<input type="checkbox"/> ChIP-seq
<input checked="" type="checkbox"/>	<input type="checkbox"/> Flow cytometry
<input checked="" type="checkbox"/>	<input type="checkbox"/> MRI-based neuroimaging

Antibodies

Antibodies used

The primary antibody of Rubisco used in this study is a rabbit polyclonal antibody against wheat Rubisco. This non-commercial Rubisco antibody was a generous gift from Emeritus Professor of Plant Molecular Biology, John C. Gray, Department of Plant Sciences, University of Cambridge, UK.
The secondary antibody is a HRP conjugated goat anti-rabbit purchased from Invitrogen. The catalog number of it is PI31466.

Validation

The capacity of this polyclonal anti-wheat Rubisco antibody to recognize the Chlamydomonas Rubisco was demonstrated previously, in western blot of total soluble proteins and immunogold labelling experiments (see <https://doi.org/10.1073/pnas.1210993109>). In our experiments, the antibody produced two bands of expected size in western blots, corresponding to the large and small subunits of Rubisco.